Numerical Computations of Wind Turbine Wakes

by

Stefan S. A. Ivanell

January 2009
Technical Reports from
Royal Institute of Technology
Linné Flow Centre, Department of Mechanics
SE-100 44 Stockholm, Sweden

Front cover illustration shows a photo of Horns Rev located 15 km off the west coast of Denmark. At the time the photo was taken the pressure was close to the vaporizing pressure resulting in a visualization of the wakes behind the turbines, [UNI-FLY A/S 2008].

Typsatt i $\mathcal{AMS}$-LaTeX.

Akademisk avhandling som med tillstånd av Kungliga Tekniska Högskolan i Stockholm framlägges till offentlig granskning för avläggande av teknologie doktorsexamen torsdagen den 19:e februari 2009 kl 10:15 i sal F3, Kungliga Tekniska Högskolan, Lindstedtsvägen 26, Stockholm.

Universitetsservice US AB, Stockholm 2009

.

To Ida, Anton and Edvin

For your love and support and happy smiles that after long working hours brings new energy.

S. Ivanell 2009, **Numerical Computations of Wind Turbine Wakes**

Linné Flow Centre, KTH Mechanics
SE-100 44 Stockholm, Sweden

Abstract

Numerical simulations of the Navier-Stokes equations are performed to achieve a better understanding of the behaviour of wakes generated by wind turbines. The simulations are performed by combining the in-house developed computer code EllipSys3D with the actuator line and disc methodologies. In the actuator line and disc methods the blades are represented by a line or a disc on which body forces representing the loading are introduced. The body forces are determined by computing local angles of attack and using tabulated aerofoil coefficients. The advantage of using the actuator disc technique is that it is not necessary to resolve blade boundary layers. Instead the computational resources are devoted to simulating the dynamics of the flow structures.

In the present study both the actuator line and disc methods are used. Between approximately six to fourteen million mesh points are used to resolve the wake structure in a range from a single turbine wake to wake interaction in a farm containing 80 turbines. These 80 turbines are however represented by 20 actuator discs due to periodicity because of numerical limitations.

In step one of this project the objective was to find a numerical method suitable to study both the flow structures in the wake behind a single wind turbine and to simulate complicated interaction between a number of turbines. The study resulted in an increased comprehension of basic flow features in the wake, but more importantly in the use of a numerical method very suitable for the upcoming purpose.

The second objective of the project was to study the basic mechanisms controlling the length of the wake to obtain better understanding of the stability properties of wakes generated by wind turbine rotors. The numerical model was based on large eddy simulations of the Navier-Stokes equations using the actuator line method to generate the wake and the tip vortices. To determine critical frequencies the flow is disturbed by inserting a harmonic perturbation. The results showed that instability is dispersive and that growth occurs only for specific frequencies and mode types. The study also provides evidence of a relationship between the turbulence intensity and the length of the wake. The relationship however needs to be calibrated with measurements.

In the last project objective, full wake interaction in large wind turbine farms was studied and verified to measurements. Large eddy simulations of the Navier-Stokes equations are performed to simulate the Horns Rev off-shore

wind farm 15 km outside the Danish west coast. The aim is to achieve a better understanding of the wake interaction inside the farm. The simulations are performed by using the actuator disc methodology. Approximately 13.6 million mesh points are used to resolve the wake structure in the park containing 80 turbines. Since it is not possible to simulate all turbines, the 2 central columns of turbines have been simulated with periodic boundary conditions. This corresponds to an infinitely wide farm with 10 turbines in downstream direction. Simulations were performed within plus/minus 15 degrees of the turbine alignment. The infinitely wide farm approximation is thus reasonable. The results from the CFD simulations are evaluated and the downstream evolution of the velocity field is depicted. Special interest is given to what extent production is dependent on the inflow angle and turbulence level. The study shows that the applied method captures the main production variation within the wind farm. The result further demonstrates that levels of production correlate well with measurements. However, in some cases the variation of the measurement data is caused by the different measurement conditions during different inflow angles.

Descriptors: Actuator Line Model, Actuator Disc Model, Wind Turbine Wake, CFD, LES, EllipSys3D.

Acknowledgments

This doctoral thesis is a result of cooperation between Gotland University, Visby, Sweden, The Royal Institute of Technology, Stockholm, Sweden, and The Technical University of Denmark, Copenhagen, Denmark.

I would like to thank the Swedish Energy Agency for financing the major part of this project. A special thanks to DBW for their generous grant "Sällskapet DBW:s stipendium för Högskolan på Gotland - 2005". I would also like to thank Gotland University for their economic support during parts of this project.

I wish to express my sincere thanks to my supervisor, Professor Dan Henningson at the Royal Institute of Technology, for his never ending encouraging support.

Particular thanks to my second supervisor, Professor Jens Sørensen and his colleague Robert Mikkelsen, among others, at The Technical University of Denmark, Copenhagen. We had many interesting discussions during my visits to DTU. You always made me feel welcome, thanks for that.

Special thanks to Björn Montgomerie, at The Swedish Defence Research Agency, for his enthusiastic support and many interesting discussions.

Thanks to the late Jess Michaelsen at DTU who gave me access to run my computations at the new Linux cluster and for sharing the EllipSys3D code.

Special thanks to Robert Mikkelsen for your support of the EllipSys3D and the actuator line/disc methods. Sincere thanks for all hours you spent with me during late evenings at DTU and also for the nice company during evenings in Copenhagen and during conferences at other locations.

Of course I also would like to thank my PhD-student colleagues, especially Espen Åkervik and Daniel Ahlman, at the Mechanical Department at the Royal Institute of Technology for the many interesting discussions during different courses and projects.

A special thanks to Tor Broström, head of the research and teaching board at Gotland University. You were very helpful when initializing this project and have been very supportive during the entire project. Thanks for your friendship and all interesting discussions during these years. Great thanks to Kjell Larsson, who was the head of the department (at Gotland University) during the major part of this project, for your encouragement and support during the entire project. Thanks to Inga-Märit Koehler for proofreading.

And last, I would like to express my sincere thanks to my colleagues at Gotland University, who provided me with a very nice and friendly environment and also for a great understanding when I concentrated my time on the research in this project, even when the workload in other projects was high.

Tack käre Mor, Far och Storasyster för allt stöd genom åren. Tack min underbara fru för all kärlek och all förståelse för alla resor som detta projekt inneburit.

Visby, January 2009

Stefan S. A. Ivanell

Preface

This thesis consists of two parts. In part 1 an introduction to the topic is presented, whereas part 2 contains the papers. A short description of each paper and division of work between authors is given here.

The project was initiated and defined by Stefan Ivanell (SI) and Dan Henningson (DH). The work was performed by SI under the supervision of DH and Jens Norker Sørensen (JS) in collaboration with Robert Mikkelsen (RM). In the first stage of the project Björn Montgomerie (BM), at the Swedish Defense Research Agency, was also deeply involved.

Paper 1 *Analysis of numerically generated wake structures.* Stefan Ivanell, Jens N Sørensen, Robert Mikkelsen, Dan Henningson. Wind Energy, 2009, Volume 12, Issue 1, p63-80, ISSN '1099-1824', (Published Online: Sep 18 2008, DOI:10.1002/we.285).

The simulations in Paper 1 were performed by SI with support from RM. The methods for evaluation of the circulation was introduced by SI with support from BM and JS. The paper was written by SI and JS.

Paper 2 *Stability analysis of the tip vortices of a wind turbine.* Stefan Ivanell, Robert Mikkelsen, Jens N Sørensen, Dan Henningson. Wind Energy, submitted 2009-01-15.

The method introduced in Paper 2 was developed by SI and DH. The simulations were performed by SI with support from RM. The paper was written by SI under supervision of DH and in collaboration with JS and RM. An early version of the work was presented at the 46th AIAA Aerospace Sciences Meeting and Exhibit in Reno, January 2008, and was published as an AIAA conference proceeding, AIAA-2008-1322.

Paper 3 *Three-dimensional actuator disc modelling of wind farm wake interaction.* Stefan Ivanell, Robert Mikkelsen, Jens N Sørensen, Dan Henningson. European Wind Energy Conference and Exhibition, Brussels, 2008, PO.149. www.ewec2008proceedings.info

The simulations in Paper 3 were performed by SI in collaboration with RM and under the supervision of JS and DH. The paper was written by SI under supervision of RM, JS and DH. Paper 3 was presented as a poster with proceeding at the European Wind Energy Conference and Exhibition in Brussels, April 2008. The paper has been updated after a language check.

Paper 4 *Actuator disc modelling of wake interaction in Horns Rev wind farm.* Stefan Ivanell, Robert Mikkelsen, Jens N Sørensen, Dan Henningson. To be submitted to Wind Energy.

The simulations in Paper 4 were performed by SI in collaboration with RM and under the supervision of JS and DH. The paper was written by SI under supervision of RM, JS and DH.

Paper 5 *Validation of methods using EllipSys3D.* Stefan Ivanell, Robert Mikkelsen, Jens N Sørensen, Dan Henningson. 2008, Technical report, KTH, TRITA-MEK 2008:12.

Paper 5 was written by SI with support by RM. The simulations were performed by SI with support from RM.

The introduction presents summarized results of the project. The project can be divided into three steps, as will be defined in section 2.1 (The aim of the project). One can generally say that paper 1 covers step one, paper 2 step two and paper 3 and 4 step three of the project. Paper 5 serves as a validation of used methods in all previous papers, i.e., paper 1 to 4.

How many roads must a man walk down
Before you call him a man?
Yes, 'n' how many seas must a white dove sail
Before she sleeps in the sand?
Yes, 'n' how many times must the cannon balls fly
Before they're forever banned?
The answer, my friend, is blowin' in the wind,
The answer is blowin' in the wind.

How many times must a man look up
Before he can see the sky?
Yes, 'n' how many ears must one man have
Before he can hear people cry?
Yes, 'n' how many deaths will it take till he knows
That too many people have died?
The answer, my friend, is blowin' in the wind,
The answer is blowin' in the wind.

How many years can a mountain exist
Before it's washed to the sea?
Yes, 'n' how many years can some people exist
Before they're allowed to be free?
Yes, 'n' how many times can a man turn his head,
Pretending he just doesn't see?
The answer, my friend, is blowin' in the wind,
The answer is blowin' in the wind.

Bob Dylan (1971)

Contents

Roman letters

a	Axial induction factor	[-]
a	Perturbation amplitude	$[m]$
a'	Azimuthal induction factor	[-]
A, A_2	Turbine area	$[m^2]$
$\mathbf{A}$	Transformation matrix	[-]
b	Blade index	[-]
b	Wing span	$[m]$
b'	Imaginary wing span	$[m]$
B	Number of blades	[-]
c	Chord length	$[m]$
c_1,c_2	Parameter used in profile definition	[-]
C_d,C_D	Drag coefficient	[-]
C_l,C_L	Lift coefficient	[-]
c_m	Mean chord	$[m]$
C_p,C_P	Power coefficient	[-]
C_t,C_T	Thrust coefficient	[-]
C_{T1}	Empirical thrust coefficient	[-]
dF_D	Section drag force	$[N]$
dF_L	Section lift force	$[N]$
dF_N	Section thrust force	$[N]$
dF_T	Section torque force	$[N]$
D	Rotor diameter	$[m]$
$\mathbf{D}$	Drag force	$[N/m]$
$\boldsymbol{e}_L$	Lift unit vector	[-]
$\boldsymbol{e}_D$	Drag unit vector	[-]
$\mathbf{f}$	Body force (ACD)	$[N/m^2]$
$\mathbf{f}'$	Body force (ACD)	$[N/m^3]$
$\mathbf{f}_{body}$	Body force	$[N/m^3]$
$\mathbf{f}^b_{r\theta z}$	Body force (ACL)	$[N/m^3]$
$\mathbf{f}'_\epsilon$	Body force in field point (ACD)	$[N/m^3]$
$\mathbf{f}^b_\epsilon$	Body force in field point (ACL)	$[N/m^3]$
$\mathbf{f}^{2D,b}_\epsilon$	Body force in field point (2D smearing, ACL)	$[N/m^3]$
$\mathbf{f}^{3D,b}_\epsilon$	Body force in field point (3D smearing, ACL)	$[N/m^3]$
$\mathbf{f}^{2D}_L$	Body loading at ACL using 2D smearing	$[N/m^3]$
$\mathbf{f}^{3D}_L$	Body loading at ACL using 3D smearing	$[N/m^3]$
$\mathbf{f}^b_z$	Axial body force component for blade b	$[N/m^3]$
$\mathbf{f}^b_\theta$	Azimuthal body force component for blade b	$[N/m^3]$
$\mathbf{f}^b_{\epsilon z}$	Smeared axial body force comp. for blade b	$[N/m^3]$
$\mathbf{f}^b_\theta$	Smeared azimuthal body force comp. for blade b	$[N/m^3]$
f, f_{ph}	Physical frequency	$[Hz]$

f_c	Non-dimensional frequency	[-]
f_n	Normal loading	$[N]$
f_t	Tangential loading	$[N]$
F	Prantl's tip loss factor	[-]
$\mathbf{F}$	Loading	$[N/m]$
H_{after}	Total head behind ACD	$[N/m^2]$
H_{before}	Total head in front of ACD	$[N/m^2]$
$\mathrm{h_{hub}}$	Hub height	$[m]$
I	Calibration parameter	[-]
$\mathrm{J_{ACL}}$	Number point along ACL	[-]
k	Index in Fourier space	[-]
k	Turbulent energy	$[m^2/s^2]$
k	Wave number	$[1/m]$
L	Typical length scale	$[m]$
$\mathbf{L}$, $\vec{L}$	Lift force	$[N/m]$
$\dot{m}$	Mass flow rate	$[kg/s]$
n	Normal direction	$[m]$
nb	Number of blades	[-]
N	Number of blade sections	[-]
p	Pressure	$[N/m^2]$
p	Distance function	$[m]$
p_∞	Undisturbed pressure	$[N/m^2]$
p_2	Pressure close before turbine	$[N/m^2]$
p_3	Pressure close behind turbine	$[N/m^2]$
p_4	Pressure far behind turbine	$[N/m^2]$
P	Rotor power	$[W]$
Q	Torque	$[Nm]$
Re	Reynolds number	[-]
r	Radial position	$[m]$
$\mathrm{r_{wake}}$	Radial position of vortices	$[m]$
R	Turbine radius	$[m]$
RP	Rotor position	$[m]$
RP'	Close behind rotor position	$[m]$
R_w	Radial position in wake	$[m]$
s_{ph}	Seconds in physical space	$[s]$
s_{cp}	Seconds in computational space	[-]
s_p	Body force point	[-]
s	Radial direction	$[m]$
S	Integration path	$[m]$
Sr	Strouhal number	[-]
T	Thrust force	$[N]$
TI	Turbulence intensity	[%]
u_θ	Azimuthal velocity	$[m/s]$
u_z	Axial velocity	$[m/s]$
u	Axial velocity component	$[m/s]$

u'	rms value of turbulent fluctuations	$[m/s]$
U	Mean velocity	$[m/s]$
U_∞	Undisturbed wind speed	$[m/s]$
U_{disc}	Wind speed at rotor disc position	$[m/s]$
U_{rel}	Relative wind velocity	$[m/s]$
U_2	Wind velocity close before turbine	$[m/s]$
U_3	Wind velocity close behind turbine	$[m/s]$
U_4	Wind velocity far behind turbine	$[m/s]$
u	Radial velocity component	$[m/s]$
v	Fluid velocity	$[m/s]$
V_n	Normal velocity	$[m/s]$
V_{rel}	Relative wind velocity	$[m/s]$
W	Induced velocity	$[m/s]$
w	Boundary layer profile	$[m]$
w_0	Parameter used in profile definition	[-]

Greek letters

α	Angle of attack	[-]
γ	Azimuthal travel	[°]
γ	Tip spiral pitch angle	[°]
Γ	Circulation	$[m^2/s]$
η_ϵ	Regularization kernel	[-]
ϵ	Gaussian smearing function	[-]
ζ	Vorticity	[1/s]
θ_p	Section pitch angle	[°]
$\theta_{p,0}$	Blade pitch angle	[°]
θ_T	Twist angle	[°]
λ	Tip speed ratio	[-]
λ_r	Axial induction factor	[-]
μ	Dynamic viscosity	$[kg/ms]$
ν	Kinematic viscosity	$[m^2/s]$
ν_t	Eddy viscosity	$[m^2/s]$
ρ	Density	$[kg/m^3]$
σ	Turbine solidity	[-]
σ'	Local solidity	[-]
ω	Angular velocity	[rad/s]
Ω	Angular velocity	[rad/s]
ϕ	Relative wind angle	[°]
ϕ_{tip}	Relative wind angle at blade tip	[°]
ϕ_r	Pitch angle of tip vortices	$[rad]$
Φ_j	j:th velocity field	$[m/s]$
$\hat{\Phi}_k$	Complex eigenfunction	$[m/s]$
$\hat{\Phi}_k^m$	Complex eigenfunction along spiral	$[m/s]$

τ	Phase shift	$[^\circ]$
τ	Tangential direction	$[m]$
τ	Typical time scale	$[s]$

Acronyms

ACD	ACtuator Disc
ACL	ACtuator Line
BE	Blade Element
BEM	Blade Element Momentum
CDS	Central Difference Schemes
CFD	Computational Fluid Dynamics
CFL	Courant, Friedrichs and Lewy
DNS	Direct Numerical Simulation
DNW	German-Dutch Wind tunnels
DTU	The Technical University of Denmark
ECN	Energy research Centre of the Netherlands
FFA	The Aeronautical Research Institute of Sweden
FOI	The Swedish Defence Research Agency
HAWT	Horizontal Axis Wind Turbine
IEA	International Energy Agency
KTH	The Royal Institute of Technology
LDA	Laser Doppler anemometry
LES	Large Eddy Simulation
MEXICO	Model Rotor Experiments under Controlled Conditions
MPI	Message Passage Interface
NREL	National Renewable Energy Laboratory
PIV	Particle Image Velocimetry
QUICK	Quadratic Upstream Interpolation for Convection Kinematics
RANS	Reynolds Average Navier-Stokes
TUDelft	Technical University of Delft

Part I

Introduction

CHAPTER 1

Introduction

1.1. Historical remarks

Today wind turbines are the largest rotating machines on earth. They are also the oldest device for exploring the energy of wind on land. In fact, the only older device to utilize wind energy in general is the sailing ship. The use of wind by sailing ships dates back as far as 5000 years ago in Egypt. The first documented use of wind on land was made as early as 200 years B.C. in ancient Babylon. Wind turbines were also introduced into the Roman Empire by year 250 A.D. The first practical windmills were however used in Sistan, Afghanistan, from the 7th century, [Cutler 2004]. Wind turbines have without any doubt been very important for the evolution of modern society. The turbine will also be very important in the future when energy systems world wide must be replaced by renewable energy systems.

1.2. Operating characteristics of modern wind turbines

In this section the basic features of a modern wind turbine are described. The objective is to present a brief explanation of how a modern turbine functions, not only in an aerodynamic sense, but also in general. This section is mostly written as a brief background for readers who are familiar with aerodynamics but who lack knowledge about wind turbines in general.

In this section the focus is on the HAWT (Horizontal Axis Wind Turbine) type. There are however other types of turbines but they are not covered here since the market today is dominated by the HAWT and all work in this study has been performed on this type.

Wind turbines transform the energy in the wind to useful energy. Older turbines, like a windmill or a pump station, transformed the energy into mechanical energy. The modern turbines of today transform the energy into electric power in a transformation process consisting of many complicated steps. Modern turbines are advanced machines that use the latest available technology from many different fields, such as aerodynamics, mechanics, machine technology, power electronics, control systems, and solid mechanics, etc. If one also considers that they are the largest existing rotating machines, and that increasing size invites more complicated dynamics, the design challenge to engineers is understandable. To put size in perspective, the mass of the air passing the rotor in a few seconds corresponds to the mass of the turbine when the wind speed is favourable.

When wind is caught by the turbine blades, the blades respond to a force causing them to rotate for the same reason that airplanes fly. In other words, the aerodynamic lifting force is used to drive the rotor, thus generating shaft torque which is then transferred to the generator. Some turbines have a gearbox and some do not, depending on the type of generator.

The three most common turbine design types are described here;

- Type 1: A classic turbine with gearbox, "The Danish model".
  The shaft from the turbine is connected to a gearbox through a number

of steps, typically 3, that increase the rotational velocity of the outgoing axle, which in turn is connected to the generator. The generator itself is connected to the electrical grid. There are of course a number of different ways to construct the generator and the connection to the electrical grid, but that subject will not be covered in this short overview of design types.

- Type 2: A turbine without gearbox.
  This design features the blade axle connected directly to the generator. The low rotational velocity, being the same as the turbine, results in a much larger multi-pole generator. The need to encase the large generator leads to a larger nacelle. In fact, the multi-pole generator seems to outweigh the combination of gear box and standard 4-pole generator.

- Type 3: Hybrid.
  The hybrid type is a combination of the previous two. It does have a gearbox as type 1 but with fewer steps, typically only one. This results in a smaller gearbox, but since the RPM is increased as much as for the type 1, the generator required is larger than for type 1, but not as large as for type 2.

There are varying drawbacks with the different design types. The Danish concept, with a 3-step gearbox, has historically been prone to various gearbox problems and breakdowns, issues that continue to present date. The result has been high costs for replacement of the gearbox in many turbines. Note that this design type is here referred to as the Danish model since the Danes have lead the development of this type of turbine from the beginning. This does however not mean that the Danish manufacturers experienced more problem than other manufactures using the same design. One shall also consider that the gearbox for a wind turbine, or the turbine itself, has a running time of up to 24 hours a day for as much as 20 years. The result is a gearbox that is a complicated component to design, especially since it experiences dynamics from both ends, i.e., dynamics both from the dynamics of the wind, transformed into the gearbox by the shaft, and from the electrical grid at the other end.

The second design type, the multi-pole generator approach without any gearbox, eliminates the problem of a gearbox but instead creates a very heavy nacelle. That assembly has not been tested extensively off-shore and therefore may be subject to additional problems since this type of generator is typically less protected.

When comparing the energy losses between the two first design types they appear to be of the same order. A 3-step gearbox experiences about a 1 % loss per step while the power electronics used for the second approach corresponds to about 3 % loss. Conversely, their production efficiency appears to be simular.

The third design type is a compromise between the first two. Potential problems with the gearbox may now be reduced since it only has one step.

Normally this is a planetary step which could be considered as the most robust type. The 3-step generators normally have one first planetary step and then two parallel steps. There are however different opinions whether type 3 offers the best solution or if it creates a combination of the drawbacks from the two first design types.

Almost all modern turbines have variable angular velocity. This means that the turbine is resilient to variable wind. A sudden increase in wind speed can be absorbed by an increase in angular velocity instead of producing a large torque on the power train. The variable angular velocity therefore decreases the fatigue loading on the turbine. The variable speed also makes it possible to keep the turbine running at an optimum tip speed ratio that is keeping the best aerodynamic efficiency in a wider wind regime. Wind turbines are normally optimized for wind speeds around 10 m/s depending on particular site conditions. They can be designed for sites with high or low wind speeds, but common to both types is their capability to use as much energy from the wind as possible up to a certain level, i.e., the rated power. After that one controls the turbine to let energy pass the turbine and not overheat the generator. Normally turbines are shut down at about 25 m/s although it would be possible to design a turbine to use as much energy as possible up to that wind speed. That has however never been done since it would not be cost effective. The cost for a turbine with that level of required performance would be very high, and when considering average wind energy on a yearly basis there will not be sufficient energy to extract from high wind speeds even at sites with exceptional wind speeds. The wind is Weibull distributed around a much more moderate wind speed.

A turbine starts when the mean velocity in the wind is about 3-5 metres/second. The turbine then transforms as much energy as possible until the rated power of the generator is reached. The excess power must then be avoided somehow. There are typically three ways to do that.

- Stall control
  When stall control is used, the blades are aerodynamically designed to lose lift force at a certain angle of attack. The turbine is therefore constructed in a way to ensure that when the limit on the generator is reached the angle of attack where stall starts is reached as well. When the wind increases even more, i.e., with an increased angle of attack, the lift force of the blades also decreases because of increasing stall. Therefore, stall is achieved by maintaining constant rotor RPM while the increasing wind speed causes an increase of the radial distribution of the angle of attack.

- Pitch control
  When pitch control is used, the blades are turned (pitched) to loose lift force. The trend today is to use this method for large turbines. Modern turbines also use active pitch control where the pitch can be changed

during one revolution. This is done by controlling the bending moment of each blade. This opens new possibilities to compensate for wind shear and wakes in farms.

- Active stall
  Active stall control triggers stall intentionally. Once in stall only very small pitch excursions are required to give shorter response times than those of pitch-to-avoid stall control.

The turbine must yaw into the wind at all times. On top of the nacelle there is an anemometer and a wind vane which measures wind speed and the direction of the wind. When the wind direction changes the nacelle is turned by electric motors. These motors, typically 2 or 4, are positioned inside a cog ring at the top of the tower.

Irrespective of control system, the turbine is stopped at a critical wind speed, typically 25 m/s, for safety reasons.

All turbines have two independent brake systems. The brake systems are used for emergency stops and when maintenance is needed. The turbines are equipped with an aerodynamic and a mechanical brake. The design of the aerodynamic brake depends on the control system; a stall controlled turbine has pitchable blade tips, whearas a pitch-controlled turbine turns the whole blades.

The mechanical brake system consists of a disk brake. For turbines with a gearbox the brake is positioned on the axle, with highest rotational velocity, out from the gearbox. In that way the brake efficiency is increased, but the drawback is that if the gearbox for some reason breaks the mechanical brake will not function. For turbines without a gearbox the brake is positioned on the main axle.

When a turbine is stopped in a controlled process, the aerodynamic brake reduces the angular velocity to a great extent before the mechanical brake is applied. If an emergency occurs both brake systems are activated at the same time.

Both brake systems are ”active”, i.e., a force is acting to deactivate them. Therefore, if something goes wrong, for example a power failure, the brakes are energized automatically without any applied force or control system.

The largest turbine built today has a generator of about 5 MW. A turbine of that size, at a good on-shore wind site, will produce about 10 GWh of electrical energy per year and about 15 GWh at a good wind site off-shore. In Sweden this is sufficient to provide the energy for 500 electrically heated normal size one-family houses, for 2,000 houses with other heating system, or for 5,000 flats.

1.3. Industry trends

Today the biggest export industry in Denmark is wind turbines. The wind power industry over the last decades has shifted from small scale industries to large scale multi-national companies. During the last decade small companies have been acquired by larger firms. In addition, large companies in the energy industry, but without any historical background in wind power, have shown greater interest in the wind power industry and bought wind turbine companies. Today there is a long waiting list for turbines worldwide. The reason for this is of course that the world increasingly realizes the need to accelerate replacement of fossil fuels. Wind power has also become one of the most cost effective ways of producing energy, especially renewable energy. The wind energy industry is therefore a thriving market worldwide.

The trend during the last decades has also been that the turbine size has increased by many factors. In 1980 the power of a commercial turbine was about 50 kW with a diameter of about 15 meters. Today the best-selling machines are about 2,500 kW - 3,000 kW with a diameter of 80 to 90 meters. The largest one on the market is about 6 MW and has a diameter of about 125 meters. This is an enormous growth in functional size compared to other mechanically powered applications, such as airplanes and transport ships. Both airplanes and ships however also grew fast in size during a period before economic and infrastructure stagnation. The growth rate of turbine size will probably also slow down for similar reasons. Already today there are infrastructure problems with transporting blades to on-shore sites. Growth limits may be higher for off-shore turbines, although it is easier to transport the blades, because it is still necessary to have cranes that can lift heavy nacelles up to more than 100 meters. Another reason for decline could be the high investment in these big machines. The trend is however that small scale investments are replaced with large scale production by large energy companies. Planned wind power parks are reaching the same size as nuclear power plants. Wind turbines are no longer small scale power producers but instead large scale plants.

The Swedish government has set a goal to reach 10 TWh annular electric energy from wind power in 2015. The Swedish energy agency has also proposed a new goal of 30 TWh in 2020. This should be put in perspective with the Swedish production of 1.4 TWh in 2007. That production originated from an installed capacity of 788 MW distributed from about 900 turbines. The production from wind power contributed only 1.39 % of the Swedish total electric consumption in 2007. Denmark is the record holder, where the production from wind power was more than 20% of the total electric consumption. In Sweden there is also a unique possibility to supply a large part of the electric consumption from wind power since about 45% of the Swedish electric production originates from hydro power which is very suitable to combine with large portions of wind power because of the fast regulation possibility of hydropower. Basically, when the wind production is high, one turns down the hydro production and vice versa. Of course, the transport of energy by cables between

different locations in the country is also an issue that has to be solved since there may be bottleneck problems.

Worldwide, the installed capacity has increased 25% annually during the last 5 years and the trend continues, [GWEC 2008]. Last year the growth rate of installed capacity was greatest in Sweden, [EWEA 2008]. Of course, it is starting from a very modest level compared to other countries, but it indicates a shift in the wind power trend in Sweden.

Based on the above, one can safely say that wind power will expand worldwide and in Sweden for a long time.

CHAPTER 2

Background

2.1. The aim of the project

Knowledge of wind power technology has increased over the years. Lanchester, [Lanchester 1915], and Betz, [Betz 1920], were the first to predict the maximum power output of an ideal wind turbine. The major break-through was achieved by Glauert who formulated the Blade Element Momentum (BEM) method in 1935, [Glauert 1935], which will be discussed in section C.2.

The design codes of today are still based on the Blade Element Momentum method. It has however been extended to allow for dynamic events, with patch work and ad hoc engineering methods, sometimes of doubtful quality.

Therefore, the aerodynamic research is today shifting toward a more fundamental approach since the basic aerodynamic mechanisms are not fully understood and the importance of accurate design models increases as the turbines are becoming larger.

Recently, complete Navier-Stokes calculations have been performed and today supercomputers offer new possibilities.

The objective of this project is to evaluate existing aerodynamic simulation methods in order to run simulations that provide solutions satisfactory for evaluating the flow field behind one or a number of turbines, i.e., the wake and the wake interaction. From these simulations the basic physical behaviour of the wake will be studied. The project objectives can be divided into three groups.

- Single wake simulation

  The first aim is to find a suitable method for simulating the flow field around the turbine, and also to resolve the wake to the extent that it is possible to evaluate the flow field behind the turbine. Particular attention will be given to the circulation close behind the blades.

  This section of the project was a part of the larger AEROBIG project which involves five persons: Project Manager Björn Montgomerie, Professor Dan Henningson, Hans Ganander, Ingemar Carlén and Stefan Ivanell. The aim of AEROBIG was to develop design codes that are more accurate than existing codes. Physical features rather than empirical corrections will be utilized to a greater extent. Hans Ganander and Ingemar Carlén, Teknikgruppen, dealt with the solid mechanical aspects of the project, and Björn Montgomerie, FOI, handled the designing of the aerodynamic engineering methods. The task of this part of the project was to evaluate the circulation in the wake with the best tool available in order to reach a better understanding of the physics close behind the blades.

  Results from the AEROBIG project, other than this report, are found in the following references: [Montgomerie 2004*a*], [Montgomerie 2004*b*], [Åhlund 2004], [Carlén 2005*b*], [Carlén 2005*a*] and [Ganander 2005].

- Stability analysis

  The second aim is to understand the basic mechanisms resulting in the breakdown of the flow structure in the wake. This becomes especially important to understand when looking at interaction between turbine wakes. This knowledge becomes increasingly critical for correct placement of each turbine and spacing between each turbine in the large wind power plants being planned and built today. When building off-shore parks, there is often an area with shallow water where investors want to concentrate as much production as possible. On-shore, there are frequently some limitations on area caused by other factors. To be able to optimize the number of turbines and their positions, knowledge about the length of the wake behind each turbine is necessary. Working knowledge about the basic mechanisms behind breakdown of the distinct tip vortex is therefore important.

- Large park simulation

  The final goal is to be able to simulate an entire park. Clear perception about a suitable method and its limitations and basic mechanisms behind the breakdown of the flow structure, etc., are however necessary before setting up an advanced simulation model of a park. When that is achieved and a simulation model for an entire park is created, studies can be made not only on how to optimize one or two turbines but also on clusters of many turbines. This opens possibilities to study how local energy extraction, turbine spacing, yaw angle and park design affects total park efficiency. The results from wake interaction studies will also be important from a fatigue load point of view.

  When designing large wind farms there are many parameters to consider in optimizing cost efficiency. Off-shore the foundation cost is strongly related to water depth. The position of the turbines therefore becomes important. It is not unusual that the planner of the park has a limited area with reasonable water depth. (On-shore, similar limitations appear because of houses, urban areas, restricted areas, etc.) Therefore there is an optimization of water depth versus losses in production caused by wake interaction. The overall objective is therefore to use informaton from single wake simulations and stability analysis to determine how the production varies inside large wind farms. That knowledge will provide important guidelines on the relationship between park losses and distances between turbines inside a wind farm. That relationship will however depend on parameters such as turbulence intensity and geometry of the farm related to the main wind direction.

2.2. Related work

The basic flow features in the wake of a wind turbine have been an interesting topic during the last decades, and even though intensive research has been performed in this area basic knowledge about the flow behind a turbine is not well understood.

A distinct definition of the near and far wake was introduced by Vermeer et al., [Vermeer *et al.* 2003], i.e., where the near wake was defined as the area just behind the rotor, where the properties of the rotor can be discriminated. The near wake is followed by the far wake where the focus is placed on the influence of wind turbines in a farm situation, and modelling of the actual rotor is less important. The number of blades, blade aerodynamics and phenomena as stall, 3-D effects and tip vortices are then related to the near wake. In the far wake turbulence physics, wake interaction and topographic effects are the principal phenomena. To distinguish between the near and far wake can however be difficult in simulations since the near wake is the initial condition to the far wake.

A short overview of performed studies of wind turbine wakes will follow. The objective has been to separate performed work into experimental and computational parts and into near and far wake studies. This overview will concentrate on the near wake. However, it is sometimes difficult to separate performed studies based on that objective.

For a more extensive review of performed work in this area, see Vermeer et al, [Vermeer *et al.* 2003]. For additional far wake studies the reader is referred to Crespo et al., [Crespo *et al.* 1998].

The Reynold number that will be addressed in this section will be related to blade chord and rotational speed.

2.2.1. *Near wake studies*

A number of studies of the near wake have been carried out from the beginning of the 70s and to current date by a number of research institutes and universities such as: DTU, ECN, FFA, KTH, NREL and TUDelft.

2.2.1.1. *Experiments*

Most experiments have been performed at rather low Reynolds numbers. FOI has done extensive measurements of the wake flow, [Montgomerie & Dahlberg 2003]. Figure 2.1 shows smoke visualization done at FOI. Early experiments showing the paring up of the vortex spirals downstream in the wake have been carried out by Alfredsson and Dahlberg, [Alfredsson & Dahlberg 1979], see figure 2.2, which also was one of the first flow visualizations performed, followed by Alfredsson and Dahlberg, [Alfredsson & Dahlberg 1981]. Later, experiments based on various techniques, such as flow visualizations, hot-wire anemometry, PIV (particle image velocimetry) and LDA (laser doppler anemometry) were performed by Anderson et al., [Anderson *et al.* 1982], Savino and Nyland,

[Savino & Nyland 1985], Anderson et al., [Anderson *et al.* 1987], Eggelston and Starcher, [Eggleston & Starcher 1990], Vermeer, [Vermeer 1988], [Vermeer 1989], [Vermeer & van Bussel 1989], [Vermeer 2001], Ebert and Wood, [Ebert & Wood 1997], [Ebert & Wood 1999], [Ebert & Wood 2001], Whale et al., [Whale *et al.* 1996], Hand et al., [Hand *et al.* 2001], Shimizu and Kamada, [Shimizu & Kamada 2001], Medici, [Medici 2005] and Massouh and Dobrev, [Massouh & Dobrev 2007].

As an example, extensive measurements were recorded in the wake flow field behind a smaller turbine (0.18m) by Medici, [Medici 2005]. Medici used both two-component hot-wire anemometry and PIV to map the flow field downstream as well as upstream the turbine. From the study, it was found that the wake is meandering with a frequency corresponding to the Strouhal number.

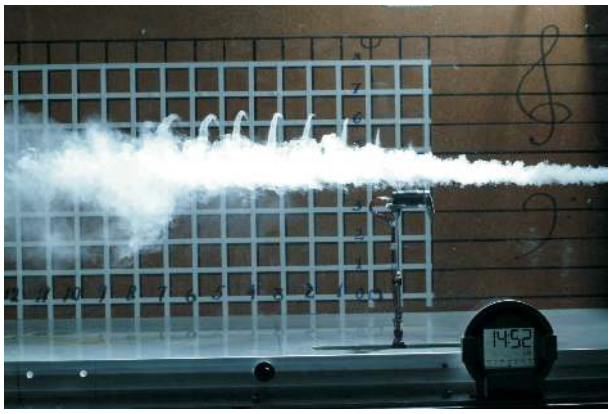

FIGURE 2.1. Wind tunnel measurement in wind tunnel LT5 at FOI, [Montgomerie & Dahlberg 2003]. See additional explanation in section 4.

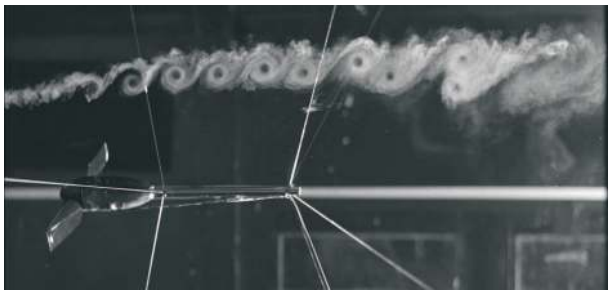

FIGURE 2.2. Wind tunnel measurement. [Alfredsson & Dahlberg 1979]. See additional explanation in section 4.

Few experiments with higher Reynolds number than 300,000 are however known, de Vries, [de Vries 1979], Anderson, [Anderson *et al.* 1982], Shimizu [Shimizu & Kamada 2001], Schreck, [Schreck 2002], Hand [Hand *et al.* 2001] and most recently the MEXICO (Model rotor EXperIments under COntrolled conditions) experiment performed in the DNW (German-Dutch Wind tunnels) wind tunnel in The Netherlands.

The test section of the MEXICO experiment was 9.5 × 9.5 m, the rotor-to-tunnel ratio was 1-3.8 and the Reynolds number was ≈ 600,000 at 75% radius. Both pressure sensors and PIV were used. There were pressure sensors at five radial positions at one of the three blades. The PIV was used to resolve chosen areas of the flow field including the wake. The PIV image could be seen in real time, therefore it was possible to identify the core of the tip vortex at different positions. Each image therefore shows the vortex core with the core approximately centred in the PIV image. These recently received data are a breakthrough in available wake data since it gives PIV images of the wake flow behind a turbine with a blade radius of about 2.25 m and a relatively high Reynold number. Since the blade also has pressure sensors it should be possible to find a correlation between the blade circulation and the wake properties. For the first time it will also be possible to trace the circulation of the tip vortex downstream in azimuthal angle based on experimental data for high Reynolds numbers. Unfortunately, it was not possible to follow the tip vortex to the extent of its breakdown due to limits in the mechanical setup of the PIV test section. Therefore there are still no experimental data on the breakdown of the tip vortex for high Reynold numbers to compare with stability simulations. The MEXICO project will however be followed up by an IEA project, the MEXNEXT project, which will concentrate on evaluating data from the MEXICO project and to verify simulation models based on these data. Hopefully the future will give us the possibility to verify numerical methods also in the regime of the break down of the vortices.

There is only one known experiment with full scale rotor (radius ≈ 5 m); the NREL Unsteady Aerodynamic Experiment in the NASA-Ames wind tunnel, [Schreck 2002], [Hand *et al.* 2001]. The test section of the NREL experiment was 24.4 × 36.6 m, the rotor-to-tunnel ratio was 1-10.8, and the Reynolds number based on chord and relative velocity was ≈ 1,000,000. Data from that measurement were the starting point for the IEA Annex XX: HAWT Aerodynamics and Models from Wind Tunnel Measurements. The emphasis of this project was however not to make wake measurements. Therefore, when evaluating the flow field behind the rotor this experiment does not make a significant contribution to knowledge.

2.2.1.2. *Computations*

All existing models to predict performance and loading are still based on the Blade Element Momentum method (BEM). It has however been extended, to allow for dynamic events, with patch work and add hoc engineering methods.

The method is also based on empirical input which is not always available or accurate.

When looking at realistic operating conditions of atmospheric turbulence, wind shear, changes in wind directions in both time and in space, wake effect from neighbouring turbines, and stall etc., it is extremely difficult to predict the power output. Existing models using the BEM method do not therefore determine the performance of a modern large turbine within an acceptable accuracy, mostly because the 3-D effects are increasingly large. Sørensen, [Sørensen 1986], showed, by a viscous-inviscid interaction technique, that the maximum lift might increase more than 30 % due to inclusion of rotational effects. This has also been confirmed in experiments by Butterfield, [Butterfield 1989], Ronsten, [Ronsten 1991] and Madsen and Rasmussen, [Madsen & Rasmussen 1991].

To overcome limitations of the BEM method, numerical methods can, in principle, provide a full description of the flow field. Models have been developed ranging from those based on potential flow and vortex theory to the most recent models that solve the Navier-Stokes equations. This overview will concentrate on the last one.

In recent times, full CFD (Computational Fluid Dynamics) simulations have been performed on wind turbines. In order to understand the basic aerodynamics of wakes and to analyse experimental data it is necessary to perform numerical simulations, either by vortex wake models or by full field Navier-Stokes CFD methods. Recent wake studies based on various CFD techniques have been presented by Sørensen et al., [Sørensen *et al.* 2007], Wußow et al., [Wußow *et al.* 2007], Walther et al., [Walther *et al.* 2007], Watters and Masson, [Watters & Masson 2007], Jimenez et al., [Jimenez *et al.* 2007], Zahle and Sørensen, [Zahle & Sørensen 2007], Mikkelsen et al., [Mikkelsen *et al.* 2007*a*] and Troldborg et al., [Troldborg *et al.* 2007]. A major problem of utilizing CFD methods for simulating wake flows, however, is the need to resolve many different length scales, ranging from the thickness of the blade boundary layer to the diameter of the rotor. When considering clusters of wind turbines installed in complex terrain it is also necessary to manage length scales covering the distance between the turbines and the size of the atmospheric boundary layer.

DTU and Risø, among others, have developed a full CFD code specially designed for wind turbine applications, [Sørensen 1995], [Michelsen 1992], [Michelsen 1994]. There are still limitations in grid sizes, etc., due to computer limitations. However, methods to resolve the wake well have been developed by Sørensen and Shen, [Sørensen & Shen 2002], and Mikkelsen, [Mikkelsen 2003]. These methods are based on the introduction of body forces, representing the blades themselves and therefore saving valuable computational resources locally at blade position. Therefore, the blade geometry does not need to be meshed and the boundary layer at the blades need not be resolved. The theory of these methods will not be addressed here since they will be discussed more in detail in section 5. Similar approaches using CFD methods have been

performed by Madsen, [Madsen 1996], [Madsen 1999]. Conformity between CFD-simulations using these models and large scale experiments has been documented by Sørensen et al., [Sørensen *et al.* 2002]. Recently, new methods using the body force approach to introduce an atmospheric boundary within the simulations has been implemented by Mikkelsen and colleagues, [Mikkelsen *et al.* 2007*b*], [Troldborg *et al.* 2007].

European research in the CFD area has mostly been carried out through EU-funded collaboration projects such as VISCWIND, VISCEL and KNOW-BLADE. Results from these projects have been reported by e.g., [Sørensen 1999], [Chaviaropouos *et al.* 2001], [Hansen *et al.* 1997], [Sørensen & Hansen 1998], [Sørensen & Michelsen 2000], [Hirsch 2001], [Michelsen & Sørensen 2001]. In the U.S., CFD simulations have been carried out by Duque et al., [Duque *et al.* 1999], [Duque *et al.* 2000] and by Xu and Sankar, [Xu & Sankar 1999], [Xu & Sankar 2000].

The last decade has experienced an increased demand for knowledge about wake stability, especially since wake interaction in present large farms results in decreased power production. Therefore, knowledge about relationships between flow parameters and wake lengths is required. Joukowski proposed a model for a two bladed propeller in 1912. His model basically consisted of two rotating horseshoe vortices, [Joukowski 1912]. Recent inviscid theory studies have however shown that the model by Joukovski is unconditionally unstable, [Okulov & Sørensen 2007]. Navier-Stokes simulations have indicated that the wake may be stable under some conditions, [Vermeer *et al.* 2003]. Inviscid studies by Widnall indicate three different modes; a long and a short wave instability, and a mutual inductance mode, [Widnall 1972]. The latter occurs when the pitch of the helix decreases and the neighbouring turns of the filament begin to interact strongly. Recent studies by Walther et al., [Walther *et al.* 2007], confirm the stability of the inviscid model but predict a breakdown of the vortex system due to viscosity.

CHAPTER 3

Classical Aerodynamic Models

This chapter will address the basic theory for different classical aerodynamic models. The following models will be covered:

- One-Dimensional Momentum Theory
- Ideal Horizontal Axis Wind Turbine with Wake Rotation
- Blade Element Method (BE)
- Blade Element Momentum Method (BEM)

The theory in this chapter has been summarized based on the following references: [Glauert 1935], [Freris 1990], [Burton *et al.* 2001], [Wilson 1998] and [Manwell *et al.* 2002].

3.1. Basic definitions

Reynolds number

The Reynolds number is a measure of the ratio of inertial forces ($v\rho$) to viscous forces (μ/L) and consequently it quantifies the relative importance of these two types of forces for given flow conditions.

$$Re \equiv \frac{dynamic\ pressure}{shearing\ stress} = \frac{\rho v/L}{\mu v/L^2} = \frac{\rho v L}{\mu} = \frac{vL}{\nu} \tag{3.1}$$

where ρ is the density, v is the fluid velocity, L is a characteristic length, μ is the dynamic fluid viscosity and ν is the kinematic fluid viscosity ($\rho = \mu/\nu$).

Local and tip speed ratio

The local speed ratio is defined as:

$$\lambda_r(r) = \frac{\Omega r}{U_\infty} \tag{3.2}$$

where Ω is the angular velocity, r the radial position at the blade and U_∞ the undisturbed wind speed. The tip speed ratio expresses the ratio between the tip speed and the undisturbed wind speed, i.e., when r becomes equal to R.

$$\lambda = \frac{\Omega R}{U_\infty} \tag{3.3}$$

where R is the radius of the blades. The tip speed ratio dictates the operating condition of a turbine and it affects a number of flow parameters that will be discussed later.

Induction

The axial and azimuthal interference factors are defined as the axial and azimuthal interference from the turbine.

$$a = \frac{U_\infty - U_{disc}}{U_\infty}, \quad a' = \frac{\omega}{2\Omega} \tag{3.4}$$

where a is the axial interference factor, a' is the azimuthal interference factor, U_{disc} is the velocity at the turbine disc position and ω the angular velocity change over the turbine disc.

Turbine solidity

The turbine solidity is defined as the ratio between the blade area to the area of the disc. It is the primary non-dimensional factor which describes the geometry of the turbine.

$$\sigma = \frac{Total\ blade\ area}{Disc\ area} \tag{3.5}$$

The local turbine solidity is defined in the same manner as the turbine solidity, but now defined locally at a certain radius.

$$\sigma'(r) = \frac{Bc(r)}{2\pi r} \tag{3.6}$$

where B is the number of blades, c the chord of the blades and r the radial position.

Thrust coefficient

The thrust coefficient corresponds to the relationship between the thrust and the power in the wind:

$$C_T \equiv \frac{T}{\frac{1}{2}A\rho U_\infty^2} \tag{3.7}$$

where ρ is the air density, A the turbine area, U_∞ the free stream velocity, and T the thrust of the turbine defined as $A \cdot \Delta p$ where Δp is the pressure difference across the disc, see appendix A for further details.

Power coefficient

The power coefficient corresponds to the relationship between the rotor power and the power in the wind:

$$C_p \equiv \frac{P}{\frac{1}{2}A\rho U_\infty^3} \tag{3.8}$$

where ρ is the air density, A the turbine area, U_∞ the free stream velocity, and P the rotor power defined as TU_{disc}, see appendix A for further details.

Strouhal number

The Strouhal number is a dimensionless number describing oscillating flow mechanisms:

$$Sr \equiv \frac{fL}{v} \tag{3.9}$$

where f is the frequency, L is a characteristic length and v is the velocity of the fluid.

3.2. Aerodynamic models

3.2.1. *One-dimensional momentum theory and the Betz limit*

This model, originated by Rankine, [Rankine 1865], but generally attributed to Betz, [Betz 1920], is based on linear momentum theory. Originally it was developed to predict performance of ship propellers. The model uses a tube-like control volume. A uniform "actuator disc", which creates a discontinuity of the pressure, represents the turbine.

This model utilizes a number of assumptions that makes it simple to employ. It produces findings, which at first approximations are compatible with measurements, and these results are often used as reference.

The following assumptions are used:

- The flow passing trough the disk can be separated from the rest of the flow by a well defined stream tube.
- Entirely axial flow
- Homogeneous, incompressible, steady flow
- No friction drag
- An infinite number of blades, i.e., the velocity is constant over the disk area and the thrust uniform on the disk area
- Rotation imposed on the flow as it passes through the disk is neglected, i.e., a non-rotating wake.
- The static pressure far upstream and far downstream of the rotor is equal to the undisturbed ambient static pressure, additional comments are found in section 3.2.3.

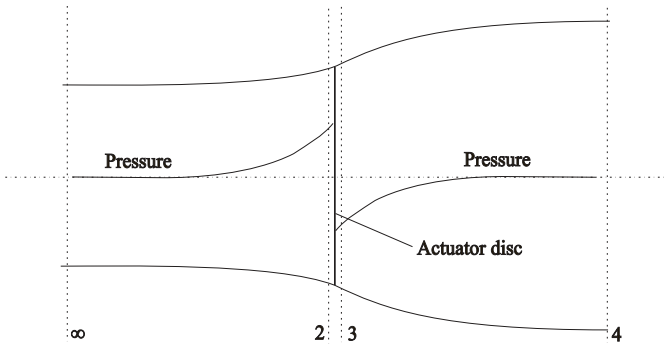

FIGURE 3.1. The actuator disc concept.

Using this model one can derive that the maximum power efficiency is $\frac{16}{27}$. This is generally referred to as the Betz limit. The derivation is considered

extraneous to this chapter and not detailed further here, instead the interested reader is referred to appendix A.

Using this model the thrust and power coefficients are:

$$C_T = \frac{\frac{1}{2}\rho A_2 U_\infty^2 \{4a(1-a)\}}{\frac{1}{2}\rho U_\infty^2 A_2} = 4a(1-a) \tag{3.10}$$

$$C_p = \frac{P}{\frac{1}{2}\rho U_\infty^3 A_2} = 4a(1-a)^2 \tag{3.11}$$

which gives a maximum C_p when $a = \frac{1}{3}$ resulting in a maximum C_p of:

$$C_{p_{max}} = \frac{16}{27} \tag{3.12}$$

In figure 3.2 it is possible to see that the highest power is reached when $a = 1/3$. Not considered here however, are effects that decrease the maximum power such as wake rotation, finite number of blades and profile drag.

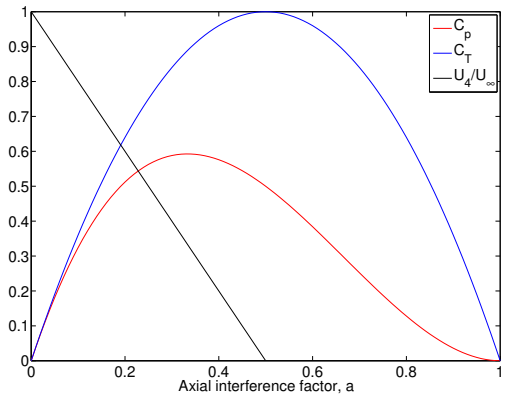

FIGURE 3.2. Momentum theory. The theory is not valid for large values of a, more comments about this are found in appendix A. U_∞ and U_4 indicate the velocity at location ∞ and 4 according to figure 3.1.

Based on figure 3.2 it is possible to realize that choosing an a slightly smaller than $\frac{1}{3}$ results in a small change in C_p-value but a rather large change in C_T-value. Therefore, from a design point of view, one may want to make a relatively large decrease in thrust for a small cost in production.

3.2.2. *Ideal horizontal axis wind turbine with wake rotation*

In the previous model the flow behind the rotor was assumed to be non-rotating. In reality, this flow rotates in the opposite direction to the rotor, as a reaction to the torque exerted by the flow on the rotor.

The energy extraction by the rotor will be less if one considers the generation of rotational kinetic energy than if one neglects it as in the previous model.

There is a close relationship between the generated kinetic energy in the wind turbine wake and the torque. The kinetic energy in the wake will be higher if the torque is higher. Therefore, a machine with low rotational speed and high torque will have higher energy losses than a machine with high rotational speed and low torque.

In this model, the control volume is divided into partial stream tubes with a radial differential extent, see figure 3.3. The energy equation can now be applied in sections before and after the blades to derive an expression for pressure difference across the blades, [Glauert 1935].

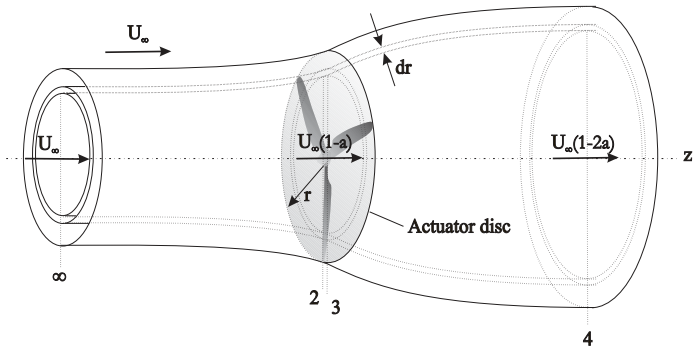

FIGURE 3.3. Control volume that moves with the angular velocity of the blades.

The following assumptions are made:

- The partial stream tubes are assumed to slide without friction, or other interference, on each other.
- The pressure in the far wake is equal to the pressure in the free stream [Wilson & Lissaman 1976]. See additional comments in section 3.2.3.
- The pressure, wake rotation and interference factors are all assumed to be a function of the radius.

The angular velocity of the air relative to the blades increases from Ω to $\Omega + \omega$ through the disk. The axial velocity on the other hand does not change as rapidly through the disk.

Using this model one can demonstrate that the power coefficient is:

$$C_{p,max} = \frac{24}{\lambda^2} \int_{a_1}^{a_2} \{ \frac{(1-a)(1-2a)(1-4a)}{1-3a} \}^2 da \tag{3.13}$$

where a_1 corresponds to $\lambda_r = 0$ and a_2 to $\lambda_r = \lambda$. The derivation has been left out of this chapter not to distract the reader with too many details. The interested reader is referred to appendix B.

The power coefficient, C_p, and the interference factors, a and a', from the two previous models have been plotted in figure 3.4.

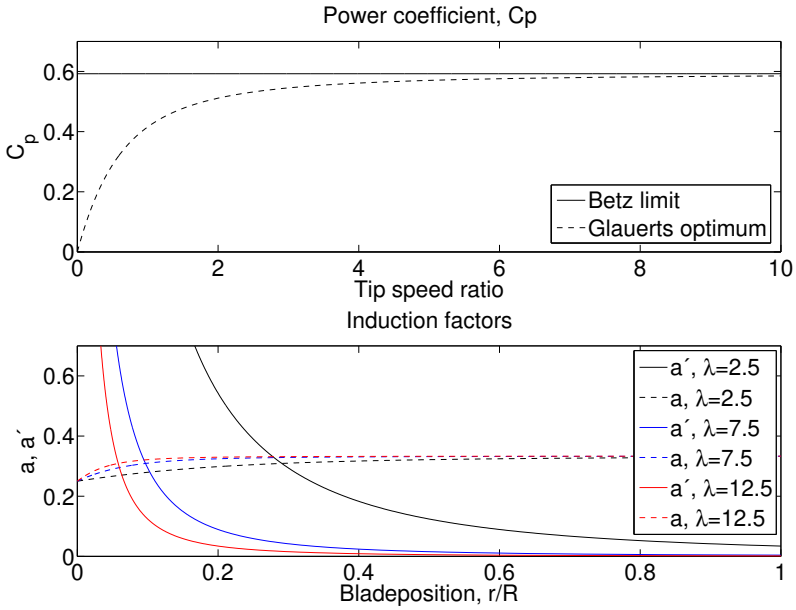

FIGURE 3.4. Power coefficient and induction factors.

When the rotation of the wake is not included, C_p is constant at $16/27 \approx 0,59$ for all tip speed ratios, this value is generally expressed as Betz limit. When considering the wake rotation, the value of the power decreases as tip speed ratio decreases, here expressed as Glauerts optimum.

The tip speed ratio for the wake rotation model has also been plotted for different blade positions in figure 3.4. The Betz axial induction factor, $a = 1/3$ corresponds well with the wake rotation model when the distance from the hub is very large, at least for larger tip speed ratios.

3.2.3. *Far wake pressure*

In previous models, the momentum balance is taken over a stream tube of the form type seen in figure 3.1. This is in principle not possible, but common in literature. In reality, the pressure varies on the mantle area of the stream tube. It is however possible to overcome this problem by considering a much larger

stream tube, where the pressure disturbance will decay as $\frac{1}{r^2}$. Normally this effect is neglected since it is small.

3.2.4. *Blade element model*

So far we modelled the turbine without considering the blades themselves. In the momentum theory the forces were derived by considering conservation of momentum.

In the blade element method the forces are expressed as functions of lift and drag coefficients. This method will however also consider the angle of attack. The basic idea is to split the blades into N sections. The forces are then calculated at each element. The total force will be given by the sum of all elements of one blade multiplied by the number of blades.

Remaining still are a number of assumptions and simplifications that must be considered.

- Firstly, the aerodynamic interaction between the blades is neglected.
- Secondly, the forces are determined only by the lift and drag characteristics of the aerofoil shape of the blades.
- Thirdly, this model also assumes that the wind is orthogonal to the plane of rotation. It is, however, possible to make the model more general so it can handle different yaw angles.

To model the forces correctly one has to carefully analyze the different forces involved. When considering the different forces, three different systems are defined; green, red and blue. See figure 3.5.

The green system represents the wind velocity. The relative wind, U_{rel}, to the blade is the result of axial and angular contributions. The axial velocity at the blade is the free stream velocity retarded to $U_\infty(1-a)$ because of the induction defined in section 3.1. The angular contribution is a combination of angular velocity $r\Omega$ and angular induction $a'r\Omega$ also defined in section 3.1.

The blue system symbolizes the blade forces orthogonal and parallel to the local wind direction. dF_L represents the lift force and dF_D represents the drag force, both at section N. Red system forces are the same as the blue system only transformed to be orthogonal and parallel to the plane of rotation. Therefore, the dF_T force represents the force contribution in angular direction from section N, i.e., useful torque. The dF_N force will in this case not produce any useful energy. It will give a thrust force to the tower.

The section pitch angle is represented by θ_p. (It is composed of the blade root pitch angle and the local twist angle.)

ϕ represents the relative wind angle, i.e., the section pitch angle plus the angle of attack, $\theta_p + \alpha$, where α is the angle of attack.

From figure 3.5 one can determine the following relationships:

$$\tan\phi = \frac{U_\infty(1-a)}{\Omega r(1+a')} = \frac{1-a}{(1+a')\lambda_r} \tag{3.14}$$

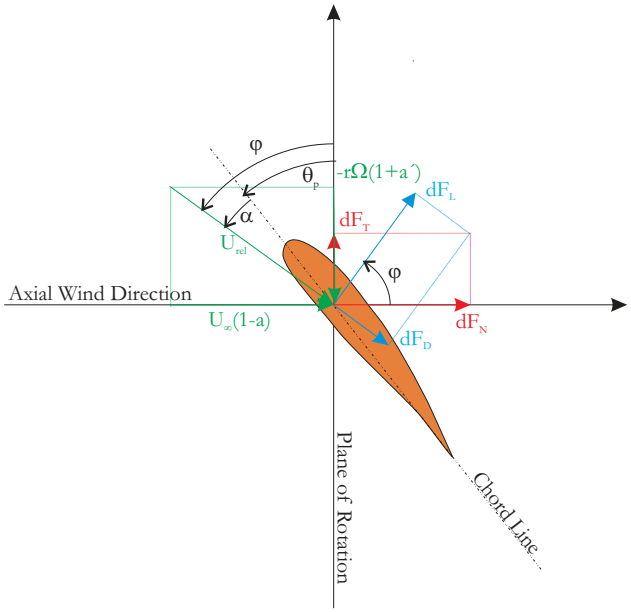

FIGURE 3.5. Definition of forces, velocities and angles.

$$U_{rel} = \frac{U_\infty(1-a)}{\sin\phi} \tag{3.15}$$

$$dF_L = C_l \frac{1}{2}\rho U_{rel}^2 c dr \tag{3.16}$$

$$dF_D = C_d \frac{1}{2}\rho U_{rel}^2 c dr \tag{3.17}$$

$$dF_N = dF_L \cos\phi + dF_D \sin\phi \tag{3.18}$$

$$dF_T = dF_L \sin\phi - dF_D \cos\phi \tag{3.19}$$

The total force will be the sum of the contributions from all sections multiplied by the number of blades, B. For one section at radius r the normal force, i.e., the force which will lead to a thrust force, will be:

$$dT = B\frac{1}{2}\rho U_{rel}^2 (C_l \cos\phi + C_d \sin\phi) c dr \tag{3.20}$$

The torque, Q, from a section at radius r will be:

$$dQ = B r dF_T = B\frac{1}{2}\rho U_{rel}^2 (C_l \sin\phi - C_d \cos\phi) c r dr \tag{3.21}$$

Equations (3.20) and (3.21) give the torque and thrust of the turbine. If these equations are combined with the momentum theory one will obtain the blade element momentum model which has been left out as non-essential information. The blade element momentum method will however be discussed together with a derivation of Betz´ optimum blade design in appendix C.

3.3. Performance

The total performance of a turbine depends on turbine type, tip speed ratio and design. The total power developed by the rotor is the total torque multiplied by the angular velocity of the rotor, i.e., $Q\Omega$. The details have been excluded here but are described in appendix D.1. Solving the equations from the blade element momentum theory, for a specific design, yields the power and torque coefficients which are functions of the tip speed ratio. Figure 3.6 illustrates a typical performance curve for a modern high-speed wind turbine compared to classic designs.

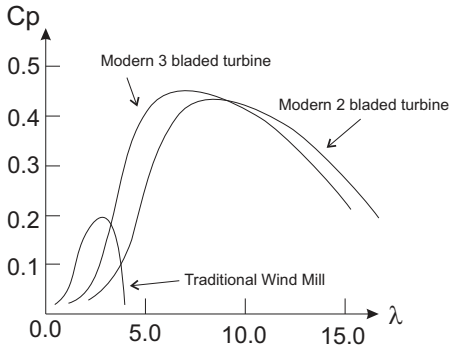

FIGURE 3.6. Cp values for a traditional wind mill compared to modern 2 and 3 bladed turbines.

The maximum power occurs when a, which normally varies with radius, approaches the Betz condition of $a = \frac{1}{3}$.

For heavily loaded turbines, when a and a' are high, the momentum and vortex theories cease to be applicable. This is because the momentum theory predicts a reversal of the flow in the wake. Since that situation cannot occur, the wake becomes turbulent and starts to entrain air from outside the wake by a mixing process which re-energizes the slow moving air that has passed through the rotor disk. An explanation of an empirical correction of the momentum theory is described in appendix D.2.

CHAPTER 4

Wake Structure

This chapter describes the flow structure in the wake. Figure 4.1 illustrates the flow structure behind one turbine with three blades. Each blade creates a tip and root vortex. Compare figure 4.1 with figure 2.1 shown in section 2.2. Figure 2.1 shows a wind tunnel experiment for a turbine with a radius of 8 centimetres. The tip spiral structure is identified by introducing smoke into the tunnel. The flow is from right to left. Since this is a two-bladed turbine, two spirals within each other are formed. One can clearly see how the smoke is captured by the two vortex spirals. At some point downstream the spiral, the structure is destroyed. Before going into the details of this complicated flow structure, a few basic features and theorems must be stated.

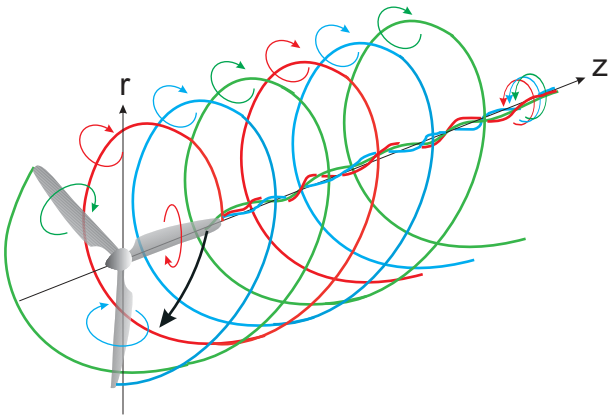

FIGURE 4.1. Since the blade tip follows a circular orbit it leaves a trailing vortex of a helical structure. The trailing tip vortex moves downstream.

4.1. Basic features and theorems

4.1.1. *Vorticity*

The vorticity is defined as:

$$\zeta = \nabla \times \vec{v} \tag{4.1}$$

A vortex can exist freely as fluid rotating around a line which can be curved or strait. The structure of an ideal vortex is such that the tangential velocity is inversely proportional to the distance from the vortex centre. This implies that the velocity at the centre is infinite. This can of course not be true. The vortex core is made up of a mass of fluid with a rigid body rotation, see figure 4.2.

The radius of the core depends upon the circumstances of the flow situation. A vortex will move freely with the general fluid motion, although it will of course contribute to the motion. The vortex can only arise in a viscous fluid.

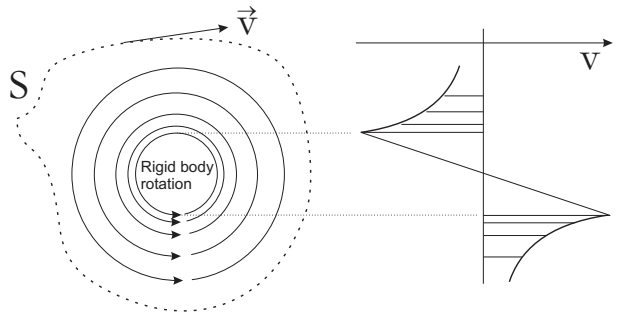

FIGURE 4.2. Vortex structure and integration path.

However, if a vortex would arise in a inviscid fluid, it would require no input of energy to sustain itself and therefore have infinite tangential velocity at the core. The core of a vortex must terminate on a solid body at each end or it must form a closed loop. In an idealized two-dimensional flow, a vortex core is assumed to be infinitely long and straight in the third dimension.

A vortex bound to a finite airplane wing or a wind turbine blade cannot simply terminate at the wing/blade tip or at the blade root. Therefore, vortex trails from each tip, or for the wind turbine also at the blade root. Theoretically, they are stretched to infinity but in practice they are dissipated by viscosity some distance behind the wing or blade, see figure 4.3.

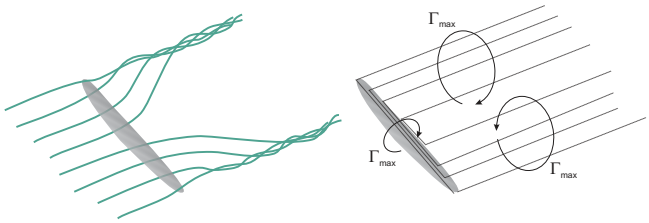

FIGURE 4.3. Left: Vortex trails from a wing. Right: Vortex trails represented by vortex lines.

A number of studies have been made in the vortex area. Dispersive and dissipative errors in numerical solutions of flow field describing a vortex that advects in constant free stream have been examined in detail by Efraimsson et al., [Efraimsson *et al.* 2005]. The long time development of an isolated wing tip turbulent vortex has been studied by RANS computations by Wallin and Girimaji, [Wallin & Girimaji 2000].

4.1.2. *Circulation*

A useful quantity in the context of induction theory is the circulation, Γ. The circulation is defined as the vorticity integrated over an open surface bounded by S:

$$\Gamma = \oint \vec{v} \cdot dS \tag{4.2}$$

where $\vec{v}$ is the velocity along the curve S which encloses the vortex, see figure 4.2.

The wake structure in the near wake is determined by the distribution of bound circulation, $\Gamma = \Gamma(r)$, along the blade. The bound circulation is according to the circulation theorem by Joukowsky related to the distribution of lift:

$$\vec{L} = \rho\vec{\Gamma} \times \vec{V}_{rel} \tag{4.3}$$

where $\vec{L}$ is the lift and $\vec{V}_{rel}$ is the relative velocity on the aerofoil section. The circulation can be computed from the lift coefficient:

$$\Gamma = \frac{1}{2} C_L V_{rel} c \tag{4.4}$$

where C_L is the lift coefficient and c is the chord length.

4.1.3. *Helmholtz' theorem*

Theoretically, the bound circulation on the blade is equal to the circulation behind the blade, i.e., in the wake. For inviscid flows, the sum of the tip and root vortices should be zero, that is however not the case for viscous flows. The tip and root vortices do however, both for inviscid and viscous flows, have a different sense of rotation, i.e., different signs of circulation. A steep decline of circulation toward the tip will lead to a rapid concentration of the vortex at the tip (occurring a few chords behind the tip). The sign of the circulation gradient along the blade will also determine the sense of rotation of the vortex behind the blade. This means if there is more than one region with a negative gradient, there will be more vortices than the tip and the root vortex, see figure 4.4.

Figure 4.4 illustrates two different distributions of circulation. The left indicates a distribution with only one area of positive and negative gradient of the circulation function. Therefore, there will only be one area of positive and negative rotations. The right figure does however show a distribution with two areas with negative and positive gradient of the circulation function. That distribution will give four vortices instead of two. The figure also exemplifies an area trailing the blade where the concentrated vortices are formed. The size of that area is illustrated by the rapidity by which full circulation strength is attained. Results will later show that this occurs at about 30° of azimuthal

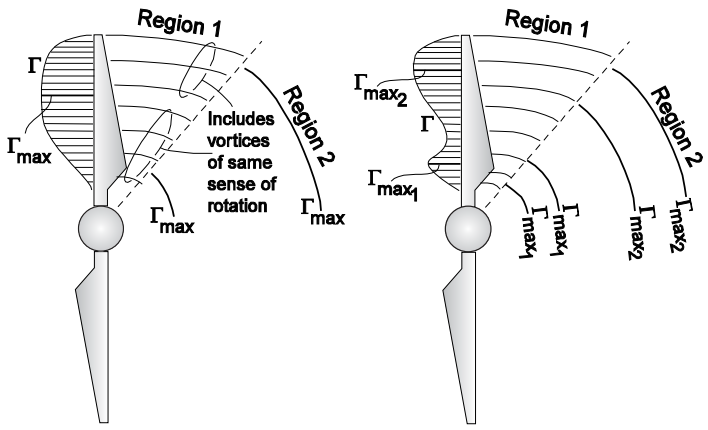

FIGURE 4.4. Trailing circulation modelling.

travel after blade passage. The root vortex concentration takes place more slowly because the radial circulation gradient is lower than at the tip.

The vortex is formed during a short time period behind the blade, see region 1 in figure 4.4. In inviscid theory the circulation for the tip and root vortices should both be equal to the maximum circulation along the blade. An explanation of that is given in figure 4.3, where it is evident that the maximum bound circulation at the wing is reached when all vortex lines along the wing are included. The circulation in the wake must therefore also correspond to that value when considering all vortex lines leaving the wing. The vortex lines do however in reality interact as shown in the left part of figure 4.3. When considering a wind turbine blade, we have the same basic behaviour, but instead of two tip vortices there is one root and one tip vortex from each blade.

In reality, the viscosity affects the vortices differently depending on the flow field. Therefore, it is not possible to make any conclusions about the dependence of the tip and root vortices other than that when neglecting viscosity, one would expect the sum of the circulation of the tip and root vortices to be approximately zero.

The tip vortices are shed into the wake in a continuous fashion and appear to emanate from a curtain radius which is slightly smaller than the radius of the turbine blade tips. The vortices also concentrate to a root vortex. Therefore it is of great interest to simulate swirl behaviour and of where the concentration toward the outer and inner vortices takes place.

Figure 4.5 again shows an example when considering a wing instead of a rotating turbine blade when replacing the continuous distribution of the circulation by a constant distribution corresponding to the Γ_{max} value. The wing can be replaced by an imaginary one with the same lift force as the physical one. The distance between the positions of the concentrated tip vortices equals

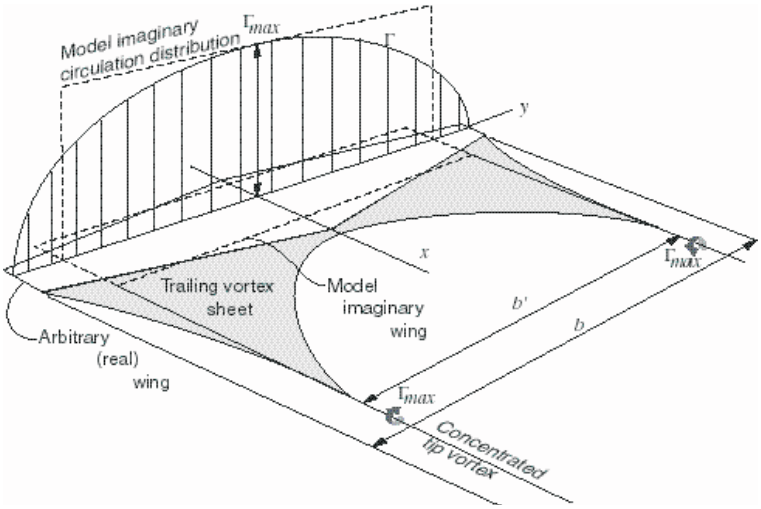

FIGURE 4.5. The figure shows where the tip vortex of a wing is located, [Montgomerie 2004a].

the span, b´, of the outer edges of the imaginary wing. A similar but more complex theory can be applied to a wind turbine case.

4.2. Wake stability

The structure of the wake and the tip and root vortices has been studied in different investigations as earlier discussed in section 2.2. Generally the root vortex structure has not been as relevant as the tip vortex structure since it is destroyed earlier because of its interaction with the induction from the hub. The three root vortices are also much closer to each other compared to the three tip vortices and the spiral structure is therefore destroyed much earlier. The stability of the tip vortex thus sets the basic behaviour of the wake. Figure 4.6 shows a field experiment performed at the Risø test centre in Denmark. The tip spiral in this case is identified by smoke exiting the blade at two radial positions close to the tip. In this case, a single blade turbine has been used to avoid disturbances from the other blades. One can clearly see how the flow is captured by the tip spiral vortex. It is also possible to see that the tip spiral starts to be unstable at a position approximately 3 rotor radii downstream of the turbine. When comparing this to figure 2.1 it is possible to see that the breakdown of that spiral system occurs at a much later downstream position. In this case the breakdown of the spiral system takes place at a position approximately 3 diameters downstream. The large difference in wake length, a factor 2, could be explained by the presence of atmospheric turbulence in the field experiment. The wind tunnel experiment is performed during more stable conditions. In figure 2.2 it is also possible to

see how the spirals start to pair up at approximately 2 diameters downstream of the turbine. Note that in this case the flow is coming from the left.

If the basic mechanisms behind this instability could be quantified, the length of the wake could be related to turbulence intensity and the frequency of wind fluctuations. The wake length has become a very important parameter during the last years with the advent of increasingly larger wind farms. When a number of turbines are positioned in close proximity there will be wake interaction, at least for some wind directions. Wake interaction affects the power output and fatigue load, and therefore the lifetime of the turbines. Wake interaction also increases in off-shore wind farms where the turbulence intensity is lower and wakes are longer since there is less turbulence to mix the flow behind the turbines. Wake interaction could therefore be less important when considering more complex or rough terrain sites. A site inside a forest, for example, could perhaps result in less wake interaction, but nevertheless one has to consider effects from a very complicated boundary layer. Today, we are far from understanding the basic features of such a complicated flow situation.

FIGURE 4.6. The figure shows a field experiment at Risø test centre, [Ioannis Antoniou and Troels Friis Pedersen 1989].

4.3. Wake interaction

Figure 4.7 shows a photo of Horns Rev wind farm. Horns Rev is located 15 km off the west coast of Denmark. The farm contains 8×10 turbines. At the time the photo was taken the pressure was close to vaporizing pressure. Even though site conditions are not well established at the time the photo was taken, one can clearly see the vaporizing behind the turbines. In the wake the flow structure is dissipated into smaller scales causing a pressure change which, in this specific case, results in vaporization. One can also observe

that for the turbine not in production (second column left from the viewer, first row), there is no vaporization. The figure provides a unique opportunity to illustrate the wake interaction in a large scale wind farm in production. It is possible to see that the flow behind the first row of turbines (in wind direction) is less turbulent compared to conditions further downstream. After the first interaction, at the position of the second row of turbines, the turbulence intensity can clearly be seen to increase. Further downstream one would expect even higher turbulence intensity, but that is however difficult to conclude from this photograph. (Compare with the photo at the front cover taken at the same time but from another direction.)

FIGURE 4.7. The figure shows a photo of Horns Rev wind farm, [UNI-FLY A/S 2008].

CHAPTER 5

Numerical Method

5.1. Flow solver

All simulations have been performed using the EllipSys3D code developed at DTU/Risø. The EllipSys3D code is a general purpose 3D solver developed by N.N. Sørensen and Michelsen, [Sørensen 1995], [Michelsen 1992], [Michelsen 1994]. The flow solver is based on a finite volume discretization of the Navier-Stokes equations in general curvilinear coordinates using multi-block topology.

The simulations have either been performed as a direct numerical simulation (DNS) or as a large eddy simulation (LES). When using the DNS approach it should be noted that we are far from resolving all scales. Therefore, a more correct term for the simulations should be implicit LES or no-model LES, since we do not resolve all scales. When using the LES approach we are employing the mixed sub-grid-scale model developed by Ta Phuoc, [Ta Phuoc 1994].

Using the coordinate directions (x_1, x_2, x_3), the Navier-Stokes equations are formulated as:

$$\frac{\partial u_i}{\partial t} + u_j \frac{\partial u_i}{\partial x_j} = -\frac{1}{\rho}\frac{\partial p}{\partial x_i} + f_{body,i} + \nu \frac{\partial u_j^2}{\partial x_j^2}, \quad \frac{\partial u_i}{\partial x_i} = 0 \tag{5.1}$$

or as:

$$\frac{\partial u_i}{\partial t} + u_j \frac{\partial u_i}{\partial x_j} = -\frac{1}{\rho}\frac{\partial p}{\partial x_i} + f_{body,i} + \frac{\partial}{\partial x_j}\left[(\nu + \nu_t)\left(\frac{\partial u_i}{\partial x_j} + \frac{\partial u_j}{\partial x_i}\right)\right], \quad \frac{\partial u_i}{\partial x_i} = 0 \tag{5.2}$$

where u_i is the velocity vector, p is the pressure, t is time, ρ is the density of air, f_{body} represents the forces acting on the blades, ν is the kinematic viscosity and ν_t the eddy viscosity that is modelled through the sub-grid-scale model, when using the LES approach. Equations (5.1) are used in the DNS approach and equations (5.2) in the LES approach. The numerical method uses a blend of third order QUICK (10%) and fourth order CDS (90%) difference schemes for the convective terms and 2nd order central difference scheme for the remaining terms.

The calculation domain consists of a number of blocks with an equal amount of points in each direction and block. The node points are distributed non-equidistant. The block size together with the number of points in each block controls how gradients are captured at critical positions.

The simulations have been performed on a Linux PC cluster at the Department of Mechanics at DTU. The cluster has been explicitly developed for EllipSys3D. It contains 210 PC's with Linux Red Hat as an operating system.

EllipSys3D is parallelized and uses MPI.

5.2. Body force approach

A full CFD simulation would require a great number of nodes at the blades to resolve the boundary layer. Therefore an approach introduced by Sørensen and colleagues is used, [Sørensen & Myken 1992], [Sørensen & Kock 1995], [Sørensen

et al. 1998], [Sørensen & Shen 2002], [Mikkelsen 2003]. This numerical method combines experiences from computational fluid dynamics (CFD) methods with experimental data by using aerofoil data. The blades are here represented by body forces representing the force distribution on the blades that act on the ambient air. The main idea is to solve the flow past a rotor without resolving the boundary layer on the blades.

Using this method, node points can be saved at the blades thus opening new possibilities for turbine simulations with a well defined wake. The drawbacks are, on the other hand, that the method is based on tabulated data from which C_L and C_D are functions of α and Re. Therefore, this method depends on the quality of the applied data. The data are taken from 2D measurements that have been modified in order to agree with experimental data.

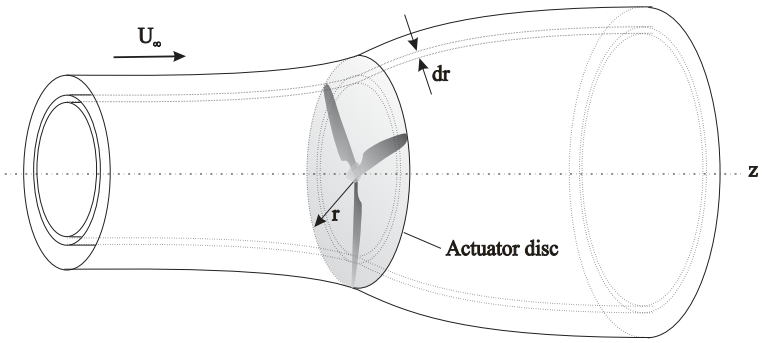

FIGURE 5.1. Actuator Disc Concept.

The presence of the rotor is modelled through body forces taken from local flow and aerofoil data. Lift and drag forces per span wise length are taken from tabulated aerofoil data as:

$$(\boldsymbol{L}, \boldsymbol{D}) = \frac{1}{2}\rho U_{rel}^2 cB(C_L \boldsymbol{e}_L, C_D \boldsymbol{e}_D) \tag{5.3}$$

where C_L and C_D are lift and drag coefficients. The unit vectors $\boldsymbol{e}_L$ and $\boldsymbol{e}_D$ are defined in the directions of lift and drag respectively. The force per span wise unit length is written as the vector sum:

$$\mathbf{F} = \mathbf{L} + \mathbf{D} \tag{5.4}$$

Two different ways of introducing the volume force approach have been used; one where the forces are smeared on to a disc, and one where the forces instead are distributed on to a line representing individual blades.

The numerical approach referred to as the actuator disc concept, see figure 5.1, has been developed by J. N Sørensen and Myken, [Sørensen & Myken 1992], N.N. Sørensen and Kock, [Sørensen & Kock 1995], J.N. Sørensen et al.,

[Sørensen *et al.* 1998] and implemented into the EllipSys3D code by Mikkelsen, [Mikkelsen 2003].

A local polar grid is introduced into which volume forces, calculated from aerofoil data, are applied.

The main limitation of the actuator disc method is that it distributes the forces evenly in the tangential direction of the actuator disc. The influence of the blades is therefore taken as an integrated quantity in the azimuthal direction. An extended three-dimensional method, the Actuator Line Method (ACL), has however been introduced by Sørensen and Shen, [Sørensen & Shen 2002], and implemented into the EllipSys3D code by Mikkelsen, [Mikkelsen 2003]. The limitation of the actuator disc method, where the influence of the blades is taken as an integrated quantity in the azimuthal direction, has now been overcome by using techniques where volume forces are distributed along lines representing each blade.

In both methods, the forces are smeared due to numerical reasons. In the actuator disc method, they are smeared in a 1D Guassian manner perpendicular to the disc. In the actuator line case they are smeared in a 2D Guassian manner in a plane perpendicular to the actuator line, at all points along the line.

When the simulation starts, an initial velocity is introduced in the entire flow field, i.e., the free stream velocity. Local velocities and angles of attack at blade positions are extracted and tabulated aerofoil data make it then possible to compute local body forces. These body forces are imported into the flow field. In the actuator disc case, the loadings are distributed on all points perpendicular to the disc because of the Guassian smearing. In the actuator line case, the loading is distributed at positions on a plane orthogonal to the actuator line, also based on the Guassian smearing. The next iteration begins, a new velocity field is reached with new local velocities and angles of attack, and so on.

5.3. Atmospheric boundary layer

When simulating large wind farms using the actuator disc method an atmospheric boundary layer is introduced. In order to impose any wind shear profile, the flow field is initially generated applying momentum sources everywhere in the domain, see Mikkelsen et al., [Mikkelsen *et al.* 2007*b*]. The magnitude of the computed momentum sources is generally very small. In practice, an initial steady computation without the wind turbines included is performed in order to establish the force field required to obtain the desired mean wind shear profile. The obtained steady force field is stored and used in unsteady simulations with wind turbines included. A power law wind shear profile with an exponent of α is chosen according to:

$$w(y) = \begin{cases} w_0 \cdot (c_2 y^2 + c_1 y) & y \leq \Delta \\ w_0 \cdot \left(\dfrac{y}{h_{hub}} \right)^{\alpha} & y > \Delta \end{cases} \tag{5.5}$$

where y is the height above the sea level, h_{hub} the hub height, and w_0, c_1 and c_2 are parameters defining the profile from the sea level to a certain height Δ. α is set to 0.15 and defines the profile above Δ set to 0.4R.

The influence of atmospheric turbulence is simulated by using a technique where turbulent fluctuations are imported in a 2D-plane upstream the rotor from a pre-generated field which the flow solver then convects downstream toward the actuator discs. See figure 5.2 where the location of the introduction of the pre-generated turbulent field is depicted by a dashed line. All pre-generated turbulent fields are generated by Manns' method, [Mann 1998], [Mann 1994], [Mann *et al.* 2002]. The simulations assume sea conditions defined by Charnock's relation, [Charnock 1955]. The turbulence intensity (u'/U) is set in the range of 2-5 percent. The use of the imposed atmospheric turbulence, by introducing time varying body forces in combination with the EllipSys3D code, was recently implemented by Troldborg et al., [Troldborg *et al.* 2007].

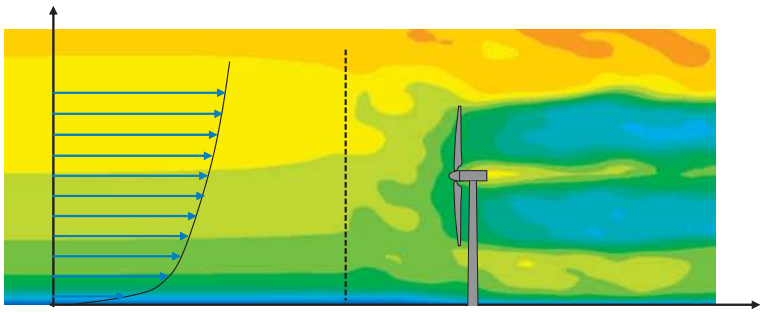

FIGURE 5.2. Conceptual idea of how the boundary layer and the atmospheric turbulence is introduced.

The output from the generation of a turbulent field using the Mann model is a spatially equidistantly spaced box where each downstream position corresponds to a timestep via Taylor´s frozen turbulence hypothesis.

Due to numerical reasons, the loading at the plane upstream the rotor is smeared in a Gaussian manner. The body force can be expressed as:

$$\mathbf{f}' = \dot{m}\mathbf{u}'_m + \rho\epsilon\frac{\partial \mathbf{u}'_m}{\partial t} \tag{5.6}$$

where $\dot{m}$ is the mass flow, ϵ a parameter that serves to adjust the smearing of the forces in a 1D manner perpendicular to the plane and $\mathbf{u}'_m$ velocity fluctuations defined from the Mann turbulence box. The smearing is done in a similar manner as earlier described in the actuator line/actuator disc method. In the present study ϵ is set equal to the size of a grid cell.

The Gaussian smearing is done by taking the convolution of the computed load $\mathbf{f}'$ and the regularization kernel η_ϵ.

$$\mathbf{f}'_\epsilon = \mathbf{f}' * \eta_\epsilon \tag{5.7}$$

where $\mathbf{f}'_\epsilon$ is the loading in each field point introducing atmospheric velocity variations and where the regularization kernel is defined as:

$$\eta_\epsilon(z) = \frac{1}{\epsilon \pi^{1/2}} \mathrm{e}^{-(p/\epsilon)^2} \tag{5.8}$$

where p is the normal distance between a grid point and the plane where turbulent fluctuations are imposed.

The resolution of the turbulence box is a factor 2 less than for the grid. Both spatial and temporal interpolations are required to reach the velocity in each point and time.

CHAPTER 6

Results and Discussion

6.1. Single wake simulation

In the first step of this project, a suitable simulation method was identified for the purpose of wake simulations behind a single wind turbine.

The method, referred to as the actuator line model (ACL) previously described in section 5, resulted in a 3D-field of the wake. The resolution of that field made it possible to analyse basic flow features of the wake. Emphasis was placed on validating the numerical method. The details of the validation have however been left out of this chapter. The interested reader is instead referred to the technical report, *Validation of methods using EllipSys3D*, (paper 5).

The flow in the wake was analysed and special interest was given to the circulation in the wake. According to classical theories, the circulation of the tip and root vortices should be conserved and equal the maximum bound circulation at the blades, as previously discussed in section 4.1.3. The result shows that the circulation of the tip and root vortices were of the same size but with different signs, all according to classical theories. The result also illustrates that the circulation of the vortices were of the same order as the bound circulation, also in agreement with the classical theories by Helmholtz.

The first step of the project was thus successful and resulted in a method where 3D-fields of the wake could be simulated. The result also shows correlation with classical theories.

Figure 6.1 shows the structure of the wake. The figure depicts pressure distribution, velocity distribution and the spiral structure here identified by iso-surfaces of the vorticity. Figure 6.1 therefore contains significant information. Data are available for the entire 3D-domain. The resolution is of course dependent on the resolution of the computational mesh. This type of field would be impossible to reach with measurements. There are however powerful measurement tools available such as PIV. Still, it would be impossible to map an entire 3D field thus indicating that CFD opens up new possibilities. CFD simulations of this size can today be made on super computers during a time period in the order of weeks. It is then possible to study the influence of different parameters by running the simulations repeatedly. The same type of wind tunnel measurements is very expensive compared to the use of supercomputers today. Modern supercomputers are commonly clusters of many standard PC machines combined in a network that allows large tasks to run on a number of processors simultaneously. However the computational code has to be written in a parallel form to allow a task to run on many processors simultaneously.

From the field plotted in figure 6.1 it is now possible to extract data for different evaluations.

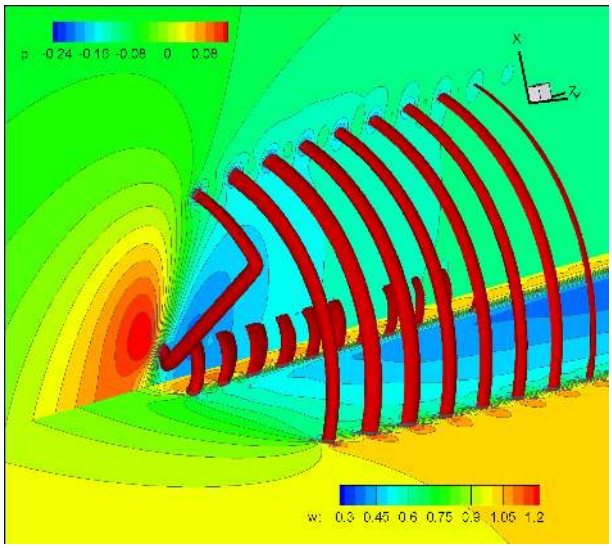

FIGURE 6.1. x=0-plane, pressure distribution; y=0-plane, streamwise velocity; iso-surface, constant vorticity.

6.2. Stability investigation

In the second part of the project, the data from the first part were used as a starting point for further investigations of basic flow features. Since the overall aim of the project is to understand how turbines interact in large wind farms, the primary task is to identify and quantify features influencing the wake structure and length. When results of these features are attained one can continue to the next step, relating wind turbine wake length with losses of production in wind farms.

A study of basic mechanisms behind the breakdown of the spiral system was initialized. The mesh was the same as in the first step of the project. The steady state simulations of that part were now used as initial conditions for time dependent simulations. At the starting point of unsteady simulations, a harmonic perturbation was introduced close behind the blade tip. The perturbation was introduced by including a body force. By changing the amplitude and frequency of that perturbation the response from the spiral system could be evaluated. The result shows that the growth rate of the introduced perturbation was dispersive, i.e., different frequency regimes resulted in different type of modes. When changing the amplitude for a specific frequency it was possible to conclude that the growth rate was not related to the perturbation amplitude, meaning that a linear growth rate could be extracted. A larger amplitude leads however to an earlier breakdown of the spiral structure since it has a larger amplitude at the starting point. This also makes it possible to relate the introduced perturbation to turbulence intensity. This analysis thus results in a relationship between the ambient turbulence and wake length. It is difficult to quantify the turbulence intensity level to a specific perturbation level, but the general physical behaviour can be explained. The result shows that the relationship between the turbulence intensity, i.e., perturbation amplitude in this case, and wake length is semilogarithmic, see figure 6.2. From figure 6.2 one can conclude that the wake length depends on the perturbation frequency which then can be related to the frequency in the ambient turbulence. The study of the influence of the perturbation frequency resulted in an identification of two types of modes. In the first mode the entire spiral system is oscillating in phase. That is, all spirals are extending from the free stream velocity in the same direction at some azimuthal position. This can occur in all three directions (axial, radial and azimuthal). The result did however show that the main extension was in axial and radial directions.

The second mode consists of out of phase motions of the spirals. This mode corresponds to the case when every second spiral extends from the free stream velocity in opposite directions at some azimuthal position. That is, every second spiral extends in positive axial or radial directions while the other spiral moves in the opposite direction at some point. When identifying different modes, the interaction of the two spiral arcs located closest together is of most interest. The complex spiral system consists of three spirals within each other but the interaction is done in pairs. Therefore, when analysing the interaction

the local interaction between the spiral arcs and its closest spiral arc is identified regardless from which of the three spirals it originates. The results show that

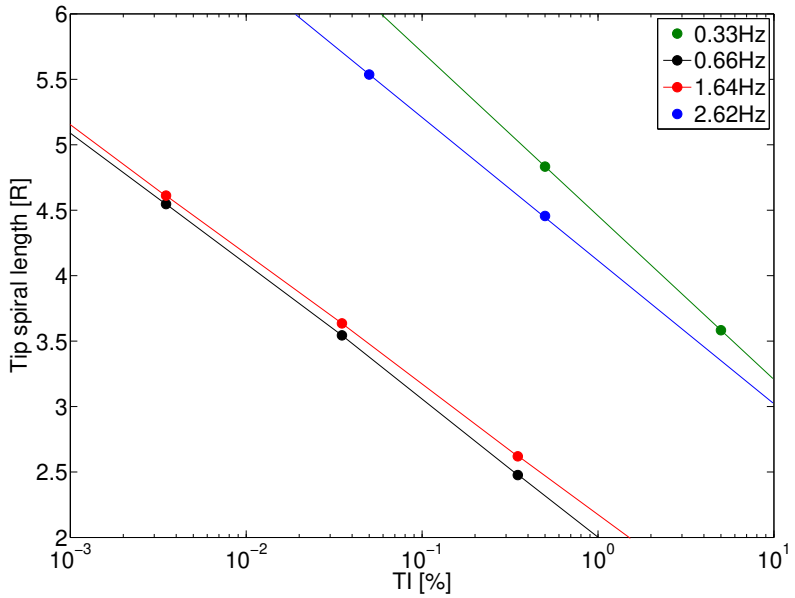

FIGURE 6.2. The figure shows the wake length related to turbulence intensity and frequency.

the mode with every second spiral out of phase results in the largest growth rate. In both cases the growth results in pairing of the vortices due to non-linear effects. The mode with every other spiral out of phase, results in an earlier breakdown of the spiral system. That mode occurs at around 0.66 and 1.64 Hz as can be identified in figure 6.2.

Figure 6.3 identifies the spiral system by an iso-surface of the vorticity. The colour coding at that surface corresponds to the axial position. The mode with every other spiral out of phase described above can clearly be identified in the figure. It is possible to see how the instability grows from about z=17.5 which corresponds to about 4 radii behind the turbine. The unit of z is $[R]$, i.e., the radius of the turbine. In this case the varicose mode has a wavelength that corresponds to 4.5 wavelengths for one revolution.

The second step of the project enhances our understanding of the basic breakdown of the wake structure and provides important data about the effect of different spacing between turbines. Collectively, this represents valuable information for moving to the third step of the project.

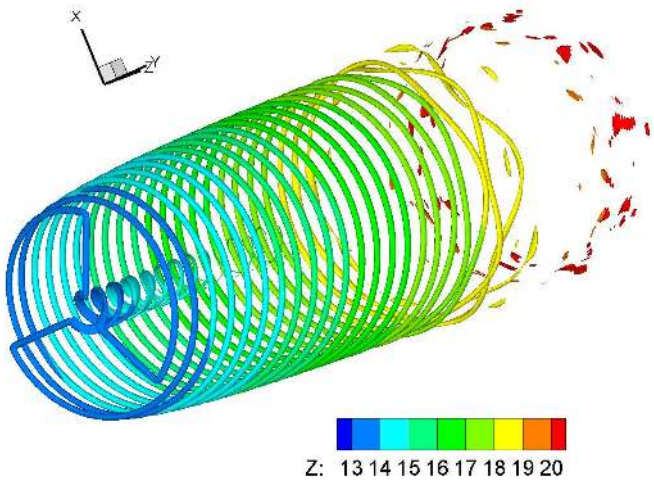

FIGURE 6.3. An iso-surface of the vorticity, f_c=5.

6.3. Farm simulation

In the last step of the project an entire wind farm with 80 turbines has been simulated. In this case the actuator disc method is used instead of the actuator line method (both methods are described in section 5). The limitation of using the actuator disc method is that individual tip vortices are not captured. The size of the simulation does however require simplification in order to handle the number of turbines. By using the actuator disc method there is still need for additional simplification since a computation with 80 turbines would be impossible to handle. Therefore, the two most central rows of turbines are simulated with periodic boundary conditions on both boundaries toward the other rows of turbines, thus assuming an infinitely wide farm. The farm simulated is the Horn Rev wind farm located 15 km off the west coast of Denmark. The farm contains 8 times 10 turbines positioned according to figure 6.4. In this simulation columns 4 and 5 are projected with periodic conditions assuming an infinitely wide wind farm. This offers a good approximation when the inflow angle is small compared to the direction of the rows. When the wind direction becomes critical, contribution from ”non existing” wind turbines outside the farm will be present. In this study we concentrate on wind directions in the regime of plus/minus 15 degrees. The error from this approximation will therefore be small since the non-existing turbines outside the farm are located approximately 18 degrees from the north boundary and 35 degrees from the south boundary to the turbines in the two centre lines that will be affected first, see figure 6.4.

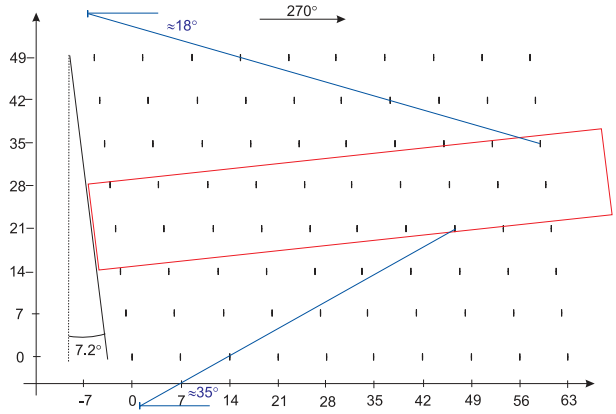

FIGURE 6.4. Layout of Horns Rev Wind Farm.

Figure 6.5 shows the flow at hub height for the three first turbines in column 5 at three different inflow angles, i.e., 265°, 270° and 285°. From the observed wake interaction it is obvious that the downstream turbines experience different flows in the three different cases depicted here.

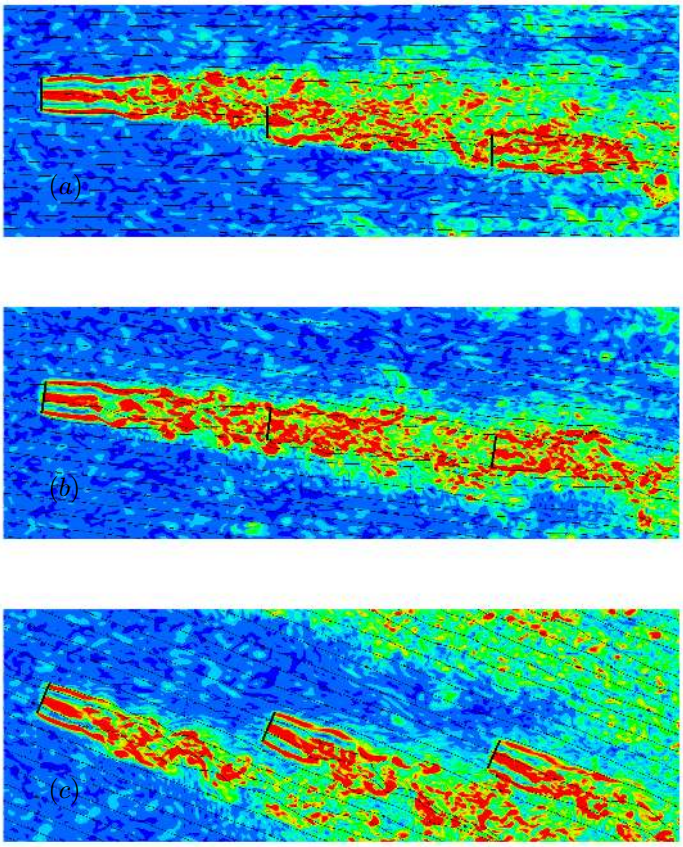

FIGURE 6.5. Vorticity at hub height. The figures illustrate different flow directions. The flow direction is identified by a number of stream-lines. (a) 265°, (b) 270°, (c) 285°.

Figure 6.6 shows a 3D field of all simulated turbines. The wakes are illustrated by an iso-surface of the vorticity. Note, that what appears to be the ground surface, is the same iso-surface as that which appears locally around each turbine and it is located at a height above the ground surface. The colour coding depicted at the iso-surface represents the pressure, the levels can be identified by the legend.

Figure 6.7 illustrates both measured and simulated results. The measured data are based on measurements in sectors of plus/minus 2.5 degrees from the simulated wind direction. The simulated results are plotted in the corresponding colour as the measured data. The simulated cases with an inflow angle of

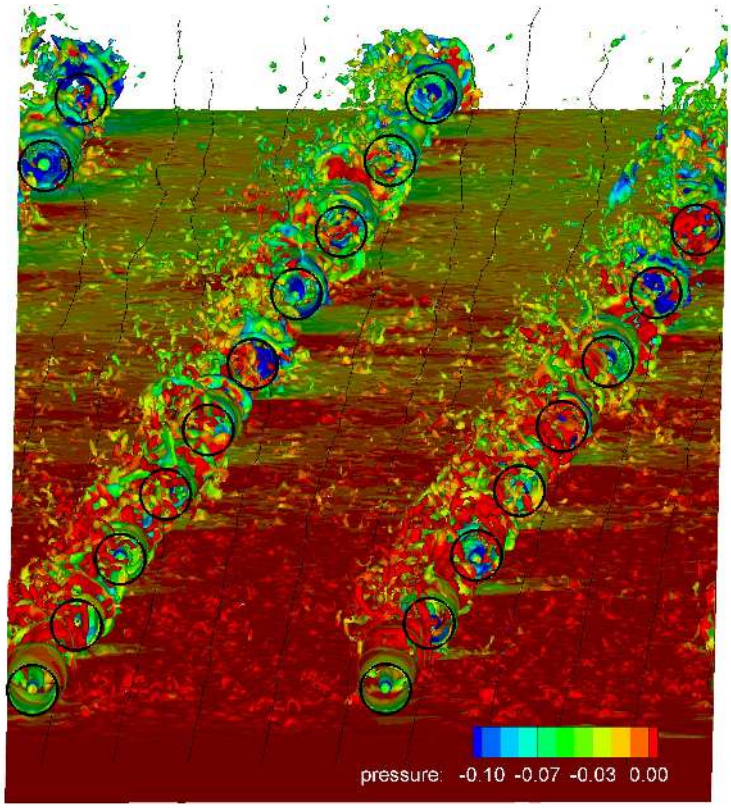

FIGURE 6.6. 3D field of the computational domain. The figure illustrates an iso-surface of the vorticity. At the iso-surface, a contour of the pressure is depicted. The turbines are here inferred by a circle.

-(5, 10 and 15) degrees are here plotted with a dotted line. Corresponding measured data are plotted with a '$*$'. The simulated cases with an inflow angle of +(5, 10 and 15) degrees are plotted with a solid line. Corresponding measured data are plotted with a '$\diamond$'. The case corresponding to full wake interaction, i.e., 270 degrees or 0 inflow angle to the column alignment, is here depicted with a solid green curve. The dot-dashed and dashed curves correspond to inflow angles of +1 and +2 degrees. These cases have been studied in order to identify the sensitivity of small deviations from the full wake case. All values have here been normalized with the production of the first turbine in wind direction.

Figure 6.8 illustrates the wake interaction in the different cases. Considering the case with an inflow angle of 285 degrees it is possible to identify how the wake interaction starts to be clearly noticeable at the fourth row of turbines,

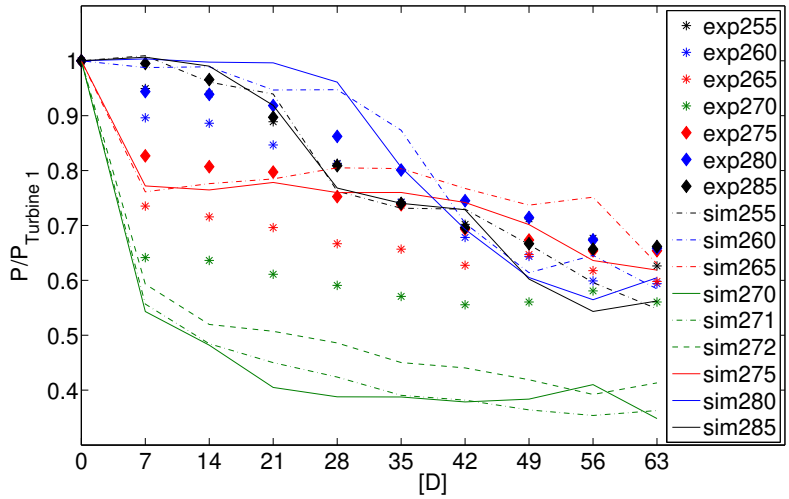

FIGURE 6.7. Simulation results compared with measurements. Results from both simulations and measurements are shown for inflow angles between 255 and 285 degrees, i.e., ± 15 degrees from the westerly direction.

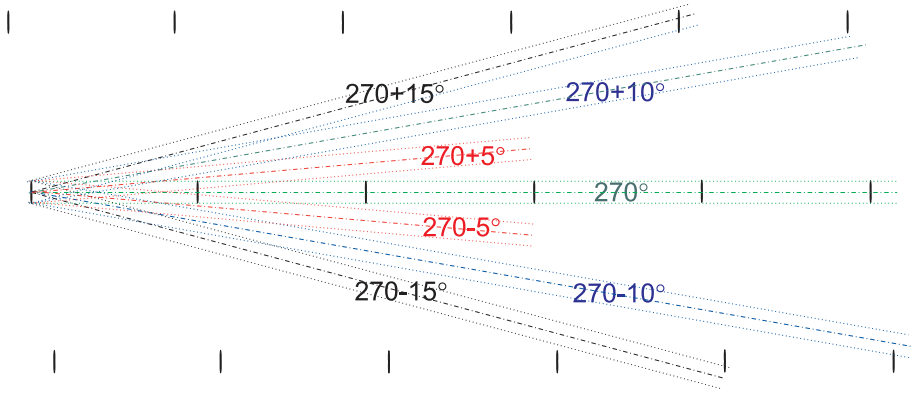

FIGURE 6.8. Wake interaction due to different wind directions.

see figure 6.7. When comparing with figure 6.8, this corresponds to the position where the wake of the first turbine is getting close to a downstream turbine. Further downstream, the production clearly drops to the next row, i.e., the fifth row, see figure 6.7. When comparing with figure 6.8, this corresponds to the point where full wake interaction occurs. Further downstream the production averages out for about three turbines, after which the production again

drops, see figure 6.7. The lowest production occurs at the ninth row, which corresponds to where the full wake interaction takes place for the second time.

When conducting the same analysis for the case with 280 degree inflow angle, one can note similar behaviour. But now the essential drop of production occurs further downstream. When comparing with figure 6.8, it is observed that the wake from the first turbine passes the fifth turbine at a greater distance than the wake from the first turbine in the 285 degree case was to the fourth turbine. Therefore, the production drop for the fifth turbine is less than the drop for the fourth turbine in the 285 degree case. It is also obvious that the production for the sixth turbine in the 280 degree case is higher than the production of the fifth turbine in the 285 degree case. This is because the 280 degree case does not have a full wake interaction, compare with figure 6.8. When comparing these two cases with measurements the simulations underestimate the wake interaction until full wake interaction occurs and overestimate the wake interaction after the point of the first full wake interaction. However, it is important to remember that measurement data are based on a sector of $\pm$ 2.5 degrees while the simulations are performed at one exact direction.

When considering the cases with an inflow angle of $\pm$ 5 degrees, i.e., the 265 and 275 degree cases, it is possible to note that both results are between the measured data at rows one to four. When looking at figure 6.8 it is also evident that an inflow angle of $\pm$ 5 degrees could not affect the measured data to the extent plotted in figure 6.7 where the production of the second row deviates about 10 % compared to the production of the first turbine. Therefore one must conclude that the circumstances of the measuring period for the cases with $\pm$ 5 degree inflow angle are very different. The simulated results are however in the same order as the measured data which should verify that the levels of the simulated production are well predicted. Further downstream the case with -5 degree inflow angle results in slightly higher values compared to the case with an inflow angle of +5 degrees. That could be explained by the geometry of the farm. The cases with north inflow angles experience a longer distance to the next turbine of the south column compared to a case where the wind is coming from the south, and the distance to the next turbine in the north column is shorter. Full wake interaction would occur at about the eleventh row in the -5 degree case, however this case has only 10 rows so the effect will be small. The last drop in the -5 degree case, i.e., between the ninth and tenth rows, may however be influenced by the wake from the first turbine.

When considering the full wake case, the 270 degree case, it is clear that the simulation overestimates the wake interaction. However, when considering that the measured data are based on a sector of $\pm$ 2.5 degrees and also comparing with a simulation using inflow angles of +1 and +2 degrees, the overestimation does not appear to be as large as first predicted.

CHAPTER 7

Conclusions

In step one of this project the objective was to find a suitable numerical method suitable to study both the flow structures in the wake behind a single wind turbine and to simulate complicated interaction between a number of turbines. In this first step approximately five million mesh points were used to resolve the wake structure in a 120 degree domain behind the turbine. The study resulted in increased comprehension of basic flow features in the wake, but more importantly it resulted in the use of a numerical method very suitable for the upcoming purpose.

The introduced simulation method was performed by combining the in-house developed computer code EllipSys3D with the actuator line and disc methodologies. In the actuator line and disc methods the blades are represented by a line or a disc on which body forces representing the loading are introduced. The body forces are determined by computing local angles of attack and using tabulated aerofoil coefficients. The advantage of using the actuator line or disc techniques is that it is not necessary to resolve blade boundary layers. Instead, the computational resources are devoted to simulating the dynamics of the flow structures.

The second objective of the project was to study the basic mechanisms controlling the length of the wake to obtain better understanding of the stability properties of wakes generated by wind turbine rotors. To determine the stability properties of wind turbine wakes a numerical study on the stability of the tip vortices behind the Tjaereborg wind turbine was carried out. The numerical model is based on large eddy simulations of the Navier-Stokes equations using the actuator line method to generate the wake including tip vortices. To determine critical frequencies the flow is disturbed by inserting a harmonic perturbation. The results showed that instability is dispersive and that growth occurs only for specific frequencies mode types. The study also provides evidence of a relationship between the turbulence intensity and the length of the wake. The relationship however needs to be calibrated with measurements.

In the last project objective, full wake interaction in large wind turbine farms were studied and verified to measurements. Large eddy simulations of the Navier-Stokes equations are performed to simulate the Horns Rev off shore wind farm 15 km outside the Danish west coast. The aim is to achieve a better understanding of the wake interaction inside the farm. The simulations are performed by combining the in-house developed computer code EllipSys3D with the actuator disc methodology. Approximately 13.6 million mesh points are used to resolve the wake structure in the park containing 80 turbines. Since it is not possible to simulate all turbines, the 2 central columns of turbines have been simulated with periodic boundary conditions. This corresponds to an infinitely wide farm with 10 turbines in downstream direction. Simulations were performed within plus/minus 15 degrees of the turbine alignment. The infinitely wide farm approximation is thus reasonable. The results from the CFD simulations are evaluated and the downstream evolution of the velocity field is depicted. Special interest is given to what extent the production is

dependent on the inflow angle and turbulence level. The study shows that the applied method captures the main production variation within the wind farm. The result further demonstrates that levels of production correlate well with measurements. However, in some cases the variation of the measurement data is caused by the different measurement conditions during different inflow angles.

Overall, the project resulted in increased knowledge about the flow structure behind wind turbines and the interaction of a number of turbines. The project also established numerical methods utilizing possibilities to simulate production variation inside large wind farms, a necessary requirement in order to optimize the large wind turbine farms of the future. A third result of the study demonstrated a relationship between turbulence intensity and wake length, making it possible to optimize the spacing between turbines in wind farms. Collectively, the conclusion established new simulation possibilities for the next generation of wind farm development. However, since these simulation methods are dependent on large computers and still demand extensive simulations, future work should concentrate on implementing these methods using an engineering approach to industrial codes. This does, however, require further development and especially computer resources to simulate more cases than have been possible within this project, i.e., to run simulations of a number of velocities and turbulence intensities corresponding to more complex terrain, and verifying these simulations with measurements. Engineering methods could then be based on a database with data from a wider regime of cases. Additional understanding of what occurs during interaction between a number of turbines can be achieved by running wake interaction studies using the actuator line method, instead of actuator disc methods, utilizing the computational possibilities of tomorrow.

APPENDIX A

Betz' Limit

For steady state flow $(\rho AU)_\infty = (\rho AU)_4 = \dot{m}$ where $\dot{m}$ is the mass flow rate and the index 4 notes the position according to figure 3.1. The thrust force is therefore equal to the mass flow multiplied with the change in velocity.

$$T = \dot{m}(U_\infty - U_4) \tag{A.1}$$

Applying requirements for continuity, momentum balance, and energy balance to the flow, the thrust and power can be determined if the assumptions above are fulfilled.

Firstly, from the momentum theorem, the thrust is:

$$T = U_\infty(\rho AU)_\infty - U_4(\rho AU)_4 \tag{A.2}$$

where ρ is the air density, A the cross section area, U_∞ the free stream velocity and U_2, U_3, U_4 the velocities at different locations according to figure 3.1.

Secondly, from the pressure drop caused by the actuator disc, which represents the turbine, the thrust can also be derived by using the Bernoulli principle separately on each side of the turbine.

In the stream tube upstream of the disc:

$$p_\infty + \frac{1}{2}\rho U_\infty^2 = p_2 + \frac{1}{2}\rho U_2^2 \tag{A.3}$$

In the stream tube downstream of the disc:

$$p_3 + \frac{1}{2}\rho U_3^2 = p_4 + \frac{1}{2}\rho U_4^2 \tag{A.4}$$

Since two of the assumptions for this model are that $p_\infty = p_4$ and that the velocity across the disc remains the same ($U_2 = U_3$), the thrust can also be expressed as:

$$T = A(p_2 - p_3) \tag{A.5}$$

If one solves equations (A.3) and (A.4) for $(p_2 - p_3)$ and substitutes that into (A.5) one obtains:

$$T = \frac{1}{2}\rho A_2(U_\infty^2 - U_4^2) \tag{A.6}$$

Combining (A.1) and (A.6) gives:

$$\dot{m}(U_\infty - U_4) = \frac{1}{2}\rho A_2(U_\infty^2 - U_4^2) \tag{A.7}$$

Recognizing that $\dot{m} = \rho A_2 U_2$ or $\dot{m} = \rho A_3 U_3$ (index 2 will be used for the disc from now on), the result generally known as Froude's theorem is obtained.

$$U_2 = \frac{U_\infty + U_4}{2} \tag{A.8}$$

The interpretation of this expression is that the velocity at the disc is the average of the free stream and far wake velocities, so the total velocity change from free stream to far wake is twice the change from free stream to the disc.

Now introducing the axial interference factor which is a measure of the turbine influence to the wind (induced velocity) and defined as:

$$a = \frac{U_\infty - U_2}{U_\infty} \tag{A.9}$$

which gives:

$$U_2 = U_\infty(1 - a) \tag{A.10}$$

$$U_4 = U_\infty(1 - 2a) \tag{A.11}$$

The theory is applicable when a is between 0 and 0.5 since the velocity has slowed to zero behind the rotor for higher values, which is physically impossible. In fact, the theory breaks down at about a = 0.35.

Power is equal to the thrust times the velocity at the disc.

$$P = \frac{1}{2}\rho A_2(U_\infty^2 - U_4^2)U_2 = \frac{1}{2}\rho A_2(U_\infty - U_4)(U_\infty + U_4)U_2 \tag{A.12}$$

substituting equations (A.10) and (A.11) gives:

$$P = \frac{1}{2}\rho A_2 U_\infty^3 4a(1 - a)^2 \tag{A.13}$$

Using equation (3.8) gives the power coefficient for the actuator disc:

$$C_p = \frac{P}{\frac{1}{2}\rho U_\infty^3 A_2} = 4a(1 - a)^2 \tag{A.14}$$

The power coefficient corresponds to the rotor power divided by the power in the wind. If we put $\frac{dC_p}{da} = 0$ we will get a for maximum C_p.

$$\frac{dC_p}{da} = 4(1 - a)^2 - 8a(1 - a) = 4(1 - 4a + 3a^2) = 0 \tag{A.15}$$

which gives a maximum C_p when $a = \frac{1}{3}$

$$C_{p_{max}} = \frac{16}{27} \tag{A.16}$$

The results demonstrate that with the given assumptions, the maximum theoretical power production is 16/27 of the power in a circular stream-tube with a constant cross section area equal to the disc area. If the free stream velocity is U_∞, then the velocity at the disc is $\frac{2}{3}U_\infty$ and at the end of the stream tube it is $\frac{1}{3}U_\infty$. Therefore, due to continuity, the tube has a cross section area that is 2/3 of the disc area upstream of the disc and twice the disc area downstream. $C_{p_{max}}$ is generally known as the Betz limit.

The thrust force can be expressed in a similar manner as the power. The non-dimensional thrust coefficient corresponds to the thrust force divided by the dynamic force and can be expressed as:

$$C_T = \frac{T}{\frac{1}{2}\rho U_\infty^2 A_2} \tag{A.17}$$

Combining equations (A.6) and (A.11) gives:

$$T = \frac{1}{2}\rho A_2 U_\infty^2 \{4a(1-a)\} \tag{A.18}$$

resulting in:

$$C_T = \frac{\frac{1}{2}\rho A_2 U_\infty^2 \{4a(1-a)\}}{\frac{1}{2}\rho U_\infty^2 A_2} = 4a(1-a) \tag{A.19}$$

APPENDIX B

Glauerts' Optimum

Bernoulli's equation can be applied to each side of the turbine disc. Let u and v be respectively the axial and radial components of the fluid velocity.

$$H_{before} = p_\infty + \frac{1}{2}\rho U_\infty^2 = p_2 + \frac{1}{2}\rho(u_2^2 + v_2^2) \tag{B.1}$$

$$H_{after} = p_2 - p' + \frac{1}{2}\rho(u_3^2 + v_3^2 + \omega_3^2 r_3^2) = p_4 + \frac{1}{2}\rho(u_4^2 + \omega_4^2) \tag{B.2}$$

where H_{before} and H_{after} indicate the total head before and after the turbine disc and p' the pressure difference across the disc.

$$H_{after} - H_{before} = -p' + \frac{1}{2}\rho\omega_3^2 r_3^2 \tag{B.3}$$

which shows that the decrease of total head, on passing through the turbine disc, exceeds the trust per unit area p' by a small term representing the kinetic energy of the rotational motion imparted to the fluid by the torque of the turbine. The expression for the total pressure head also gives:

$$p_\infty - p_4 = \frac{1}{2}\rho(u_4^2 - U_\infty^2) + \frac{1}{2}\rho\omega_4^2 r_4^2 - (H_{after} - H_{before}) \tag{B.4}$$

$$p_\infty - p_4 = \frac{1}{2}\rho(u_4^2 - U_\infty^2) + \frac{1}{2}\rho(\omega_4^2 r_4^2 - \omega_3^2 r_3^2) - p' \tag{B.5}$$

Applying Bernoulli's equation to the flow relative to the turbine blades, which are rotating with the angular velocity Ω, the relative angular velocity increases from Ω to $(\Omega + \omega)$ and consequently the decrease of pressure is:

$$p' = -\rho(\Omega + \frac{1}{2}\omega)\omega r^2 \tag{B.6}$$

The resulting thrust on an annular element, dT, is:

$$dT = (p_2 - p_3)dA = \left\{\rho(\Omega + \frac{1}{2}\omega)\omega r^2\right\} 2\pi r dr \tag{B.7}$$

We now introduce the angular interference factor, which is defined in the same manner as the axial interference factor, but now only for the angular component.

$$a' = \frac{\omega}{2\Omega} \tag{B.8}$$

The induced velocity at the rotor now consists of two components, i.e., the axial and angular components. The axial component is still aU_∞, the angular component can be expressed as $r\Omega a'$.

The expression for thrust now becomes:

$$dT = 4a'(1+a')\frac{1}{2}\rho\Omega^2 r^2 \pi r dr \tag{B.9}$$

The thrust force was in the linear momentum model determined to be $\frac{1}{2}\rho A U_\infty^2\{4a(1-a)\}$ which gives dT to:

$$dT = 4a(1-a)\frac{1}{2}\rho U_\infty^2 2\pi r dr \tag{B.10}$$

Now combining the two expressions for thrust gives:

$$\frac{a(1-a)}{a'(1+a')} = \frac{\Omega^2 r^2}{U_\infty^2} \tag{B.11}$$

The tip speed ratio, λ, is defined as the ratio of the blade tip speed to the the free stream wind speed.

$$\lambda = \frac{\Omega R}{U_\infty} \tag{B.12}$$

In the same manner, the local speed ratio is defined as the ratio of the blade speed at an intermediate radius and the free stream wind speed.

$$\lambda_r = \frac{\Omega r}{U_\infty} = \frac{\lambda r}{R} \tag{B.13}$$

Equation (B.11) now becomes:

$$\frac{\Omega^2 r^2}{U_\infty^2} = \lambda_r^2 \tag{B.14}$$

Considering the conservation of angular momentum, the torque exerted on the rotor, Q, must equal the change in angular momentum of the wake. The torque on an annular area element is:

$$dQ = d\dot{m}(\omega r)(r) = (\rho U_2 2\pi r dr)(\omega r)(r) \tag{B.15}$$

Since $U_2 = U_\infty(1-a)$ and $a' = \omega/2\Omega$, this expression is reduced to:

$$dQ = 4a'(1-a)\frac{1}{2}\rho U_\infty \Omega r^2 2\pi r dr \tag{B.16}$$

The power generated at each element, dP, is given by:

$$dP = \Omega dQ \tag{B.17}$$

Using equations (B.17), (B.13) and (B.16) gives dP as follows:

$$dP = \frac{1}{2}\rho A U_\infty^3 \{\frac{8}{\lambda^2} a'(1-a)\lambda_r^3 d\lambda_r\} \tag{B.18}$$

The contribution to the power from each annular ring is dependent of the axial and angular interference factors and the tip speed ratio, i.e., the direction and magnitude of the airflow at the rotor plane is determined by the interference factors.

Each annular ring gives the following contribution to the power coefficient:

$$dC_p = \frac{dP}{\frac{1}{2}\rho A U_\infty^3} \tag{B.19}$$

C_p now becomes:

$$C_p = \frac{8}{\lambda^2}\int_0^\lambda a'(1-a)\lambda_r^3 d\lambda_r \tag{B.20}$$

To integrate this expression one needs to relate a, a' and λ_r. From equations (B.11) and (B.14) one gets:

$$a' = -\frac{1}{2} \pm \sqrt{\frac{1}{4} + \frac{a(1-a)}{\lambda_r^2}} \tag{B.21}$$

The double root will however only be defined for positive values. The minus sign between the two terms can therefore be neglected. C_p will reach its maximum value when $a'(1-a)$ in equation (B.20) is greatest. Substituting the value of a' into $a'(1-a)$ and extracting λ_r yields:

$$\lambda_r^2 = \frac{(1-a)(4a-1)^2}{1-3a} \tag{B.22}$$

which defines the axial induction factor as a function of the local speed ratio at maximum power. If λ_r^2 then is substituted in equations (B.13) and (B.11) the angular induction factor for maximum power as a function of the axial induction factor is obtained.

$$a' = \frac{1-3a}{4a-1} \tag{B.23}$$

Differentiation of equation (B.22) results in a relationship between $d\lambda_r$ and da at maximum power production.

$$2\lambda_r d\lambda_r = \{\frac{6(4a-1)(1-2a)^2}{(1-3a)^2}\} da \tag{B.24}$$

Substituting that into equation (A.14) gives:

$$C_{p,max} = \frac{24}{\lambda^2} \int_{a_1}^{a_2} \{ \frac{(1-a)(1-2a)(1-4a)}{1-3a} \}^2 da \tag{B.25}$$

Note that the expression only is defined for values of $a_1 > 0.25$ and $a_2 < 1/3$. a_1 corresponds to $\lambda_r = 0$ and a_2 to $\lambda_r = \lambda$.

The result is (for further details see Eggleston and Stoddard, [Eggeston & Stoddard 1987]):

$$C_{p,max} = \frac{8}{729\lambda^2} \frac{64}{5} \{ x^5 + 72x^4 + 124x^3 + 38x^2 - 63x - 12ln(x) - 4x^{-1} \}_{x=(1-3a_2)}^{x=0,25} \tag{B.26}$$

where $x = (1 - 3a)$.

APPENDIX C

Blade Shape and Blade Element Momentum Theory

C.1. Blade Shape

Before moving on to the blade element momentum method, which can be considered quite complex, a simple approximation for the blade shape is performed. This method infers the relation between blade shape and performance for the optimum Betz rotor. The method is based on the following assumptions:

- The wake rotation is neglected, i.e., a' is set to zero.
- There is no drag, $C_d = 0$.
- The effects of a finite number of blades is neglected.
- The induction factor a is 1/3 in each annular stream tube for the Betz optimal rotor.

To use this design method, the tip speed λ, the number of blades B, the radius R, and an aerofoil with known lift and drag coefficients as functions of the angle of attack must be chosen.

The angle of attack will be chosen so that the assumption $C_d = 0$ becomes as reliable as possible, i.e., the C_d/C_l term is minimized. With $a = 1/3$ the momentum theory and equation (B.10) result in:

$$dT = \frac{8}{9}\rho U_\infty^2 \pi r dr \tag{C.1}$$

and from the blade element theory equation (3.20), with $C_d = 0$ becomes:

$$dT = B\frac{1}{2}\rho U_{rel}^2 (C_l \cos\phi) c dr \tag{C.2}$$

By using equation (3.15) with $a = 1/3$, U_{rel} can be expressed as:

$$U_{rel} = \frac{2U_\infty}{3\sin\phi} \tag{C.3}$$

If equations (C.1), (C.2) and (C.3) are combined one gets:

$$\frac{C_l B c}{4\pi r} = \tan\phi \sin\phi \tag{C.4}$$

In order to relate a, a' and ϕ, equation (3.14) is used and can now be expressed as.

$$\tan\phi = \frac{2}{3\lambda_r} \tag{C.5}$$

When combining equations (C.4) and (C.5) and using that $\lambda_r = \lambda(r/R)$, it is possible to express ϕ and c as:

$$\phi = \arctan\frac{2}{3\lambda_r} \tag{C.6}$$

$$c = \frac{8\pi r \sin\phi}{3BC_l\lambda_r} \tag{C.7}$$

Betz optimum blade design can now be calculated using equation (C.6) and (C.7) together with geometrical relationships from figure 3.5.

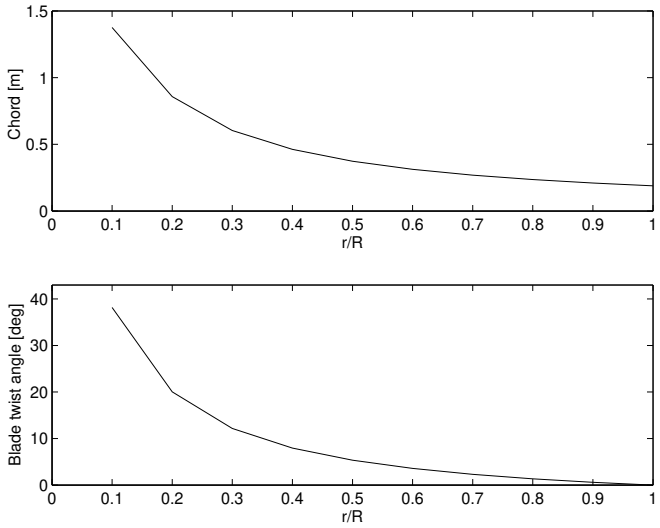

FIGURE C.1. Betz Design of a wind turbine blade.

It is evident that the blade design for an optimal Betz design has an increasingly large chord and twist angle as one gets closer to the hub.

C.2. Blade element momentum BEM model

This section will combine the results from the momentum and blade element method. If the forces from the momentum theory and blade element theory are set to be equal it is possible to derive the flow conditions for a turbine design.

The analysis starts by considering equations derived both for the momentum theory with wake rotation and the blade element theory.

From the momentum theory:

$$dT = 4a(1-a)\rho U_\infty^2 \pi r dr \tag{C.8}$$

$$dQ = 4a'(1-a)\rho U_\infty \Omega \pi r^3 dr \tag{C.9}$$

and from the blade element theory:

$$dT = B\frac{1}{2}\rho U_{rel}^2 (C_l \cos\phi + C_d \sin\phi) c dr \tag{C.10}$$

$$dQ = B r dF_T = B\frac{1}{2}\rho U_{rel}^2 (C_l \sin\phi - C_d \cos\phi) c r dr \tag{C.11}$$

The relative wind velocity in the equations from the BE-method can now be expressed in terms of the free stream velocity, using equation (3.15):

$$dT = \sigma'\pi\rho\frac{U_\infty^2(1-a)^2}{\sin^2\phi}(C_l \cos\phi + C_d \sin\phi) r dr \tag{C.12}$$

$$dQ = \sigma'\pi\rho\frac{U_\infty^2(1-a)^2}{\sin^2\phi}(C_l \sin\phi - C_d \cos\phi) r^2 dr \tag{C.13}$$

where σ' is the local solidity, defined by:

$$\sigma' = \frac{Bc}{2\pi r} \tag{C.14}$$

In the calculation of induction factors, a and a', accepted practice is to set C_d equal to zero, [Wilson and Lissaman]. This simplification introduces negligible errors for aerofoils with low drag coefficients, [Manwell et al.]. Equation (C.9) from the momentum theory and (C.13) from the BE-theory will now, with $C_d = 0$, become:

$$dQ = 4a'(1-a)\rho U_\infty \Omega \pi r^3 dr \tag{C.15}$$

$$dQ = \sigma'\pi\rho\frac{U_\infty^2(1-a)^2}{\sin^2\phi} C_l \sin\phi r^2 dr \tag{C.16}$$

The momentum theory assumes an infinite number of blades. Ignoring this, an approximation is made where equations from the momentum theory are set equal to equations from the blade element theory. This does, however, result in small errors since a' is small at the tip and at the root where it is larger, it does have a small impact because of a small torque. When the equations describing the torque from the momentum and blade element theories are set to be equal the result is:

$$\frac{a'}{1-a} = \frac{\sigma' C_l}{4\lambda_r \sin\phi} \tag{C.17}$$

When doing the same for the thrust force one gets:

$$\frac{a}{1-a} = \frac{\sigma' C_l \cos\phi}{4\sin^2\phi} \tag{C.18}$$

Equations (C.17) and (C.18) produce the following results:

$$C_l = 4\sin\phi \frac{\cos\phi - \lambda_r \sin\phi}{\sigma'(\sin\phi + \lambda_r \cos\phi)} \tag{C.19}$$

$$a = \frac{1}{1 + 4\sin^2\phi/\sigma' C_l \cos\phi} \tag{C.20}$$

$$a' = \frac{1}{4\cos\phi/\sigma' C_l - 1} \tag{C.21}$$

$$\frac{a}{a'} = \frac{\lambda_r}{\tan\phi} \tag{C.22}$$

Equation (C.22) can be given a geometrical interpretation according to figure C.2. The approximation of neglecting effects from a discrete number of blades (tip effects) only holds when the angle A between the relative and induced velocity in figure C.2 is orthogonal.

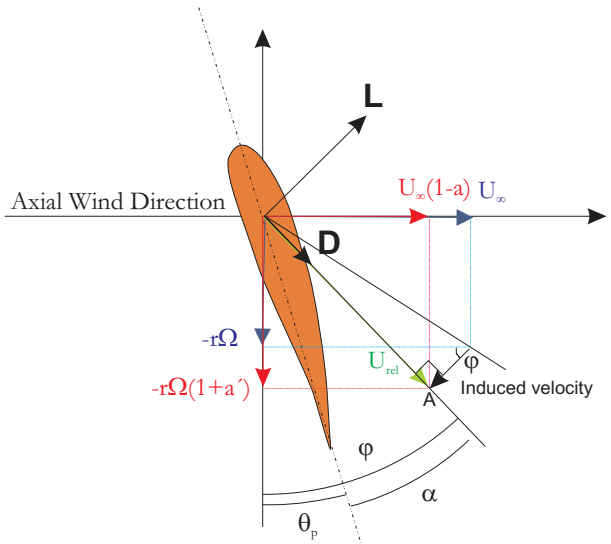

FIGURE C.2. Geometrical interpretation of equation C.22.

When not neglecting the effect of a discrete number of blades in the momentum theory, equation (C.8) must be multiplied by the Prandtl's tip correction function, F.

$$F = \frac{2}{\pi}\arccos(e^{-f}) \tag{C.23}$$

where f is defined as:

$$f = \frac{B}{2}\frac{R-r}{R\sin\phi_{tip}} \tag{C.24}$$

where B is the number of blades, R the turbine radius, and ϕ_{tip} the tip pitch angle. When introducing Prandtl's tip correction, equation (C.18) is modified to:

$$\frac{a}{1-a}F = \frac{\sigma' C_l \cos\phi}{4\sin^2\phi} \tag{C.25}$$

This expression now contains all information needed for the blade design if equation (C.22) is used as a relation between a and a' with the approximations discussed above.

APPENDIX D

Performance and break down of Momentum Theory

D.1. Performance

To determine the performance, C_p is calculated. From equation (C.15) the torque developed by the blade elements of span-wise length dr is:

$$dQ = 4a'(1-a)\rho U_\infty \Omega \pi r^3 dr \tag{D.1}$$

The drag has been excluded in this equation. When calculating the torque caused by drag, the drag must however be included. Therefore, the drag term is added to equation (D.1), see equation (C.11).

$$dQ = 4a'(1-a)\rho U_\infty \Omega \pi r^3 dr - B\frac{1}{2}\rho U_{rel}^2 c C_d \cos(\phi) r dr \tag{D.2}$$

The complete rotor will then develop a total torque Q, [Burton et al.]:

$$Q = \frac{1}{2}\rho U_\infty^2 \pi R^3 \lambda \left[\int_0^R \left(\frac{r}{R}\right)^2 \left[8a'(1-a)\frac{r}{R} - \frac{U_{rel}}{U_\infty}\frac{B\frac{c}{R}}{\pi} C_d (1+a') \right] d\left(\frac{r}{R}\right) \right] \tag{D.3}$$

The total power developed by the rotor is the total torque multiplied by the angular velocity of the rotor, i.e., $Q\Omega$:

$$C_p = \frac{Q\Omega}{\frac{1}{2}\rho U_\infty^3 \pi R^2} \tag{D.4}$$

Solving the equations from the blade element momentum theory for a specific design yields the power and torque coefficients which are functions of the tip speed ratio.

In figure 3.6 a typical performance curve for a modern high-speed wind turbine is shown.

The maximum power occurs when a, which normally varies with radius, approaches the Betz condition of $a = \frac{1}{3}$.

D.2. Breakdown of the momentum theory validity

For heavily loaded turbines, when a and a' are high, the momentum and vortex theories cease to be applicable. This is because the momentum theory predicts

a reversal of the wake flow. Since that situation cannot occur, the wake becomes turbulent and starts to entrain air from outside the wake by a mixing process which re-energizes the slow moving air that has passed through the rotor disk.

When comparing results from the momentum theory with measurements, the following approximation can be made of the thrust force coefficient. Let C_{T1} be the empirical value of C_T when $a = 1$. The empirical correction should be tangential to the momentum theory at the transition point. The equation for the empirical correction is, [Freris]:

$$C_T = C_{T1} - 4(\sqrt{C_{T1}} - 1)(1 - a) \tag{D.5}$$

and the value of a at the transition point is:

$$a_T = 1 - 0.5\sqrt{C_{T1}} \tag{D.6}$$

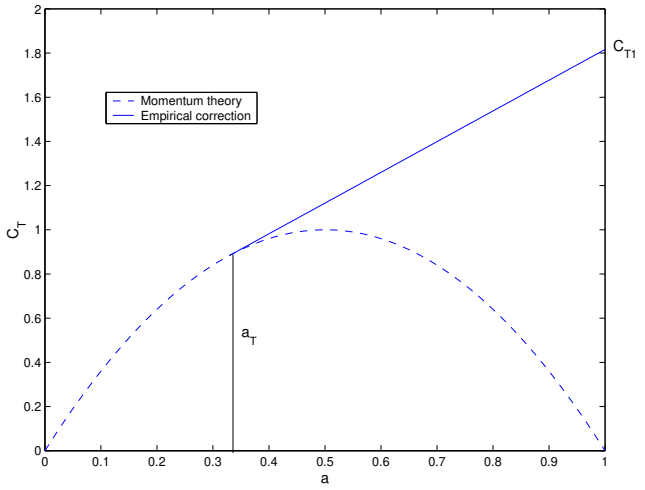

FIGURE D.1. Empirical correction to the momentum theory, $C_{T1} = 1.816$.

C_{T1} must lie between 1.6 and 2. According to Anderson, [Anderson], C_{T1} should be 1.816 for the best fit.

Bibliography

Alfredsson, P. H. & Dahlberg, J-A. 1979 A preliminary wind tunnel study of windmill wake dispersion in various flow conditions. *Tech. Rep* Technical Note AU-1499 Part 7. Swedish Defence Research agency, Stockholm Sweden.

Alfredsson, P. H. & Dahlberg, J-A. 1981 Measurments of wake intersection effects on power output from small wind turbine models. *Tech. Rep* Technical Note HU-2189, part 5. Swedish Defence Research agency, Stockholm Sweden.

Anderson, C., Niven, A., Jamieson, P., Knight, R. & Milborrow, D. 1987 Flow visaulization on rotating blades. In *9th British Wind Energy Association Conference*.

Anderson, M., Milborrow, D. & Ross, N. 1982 Performance and wake measurements on a 3 m diameter horizontal axis wind turbine, comparison of theory, wind tunnel and field test data. *Tech. Rep* Technical Note HU-2189, part 5. University of Cambridge, Department of physics, Cavendish Lab., Cambridge U.K.

Betz, A. 1920 Das maximum der theoretisch möglichen ausnützung des windes durch windmotoren. *Zeitschrift das gesamte Turbinewessen* pp. 307–309.

Burton, T., Shape, D., Jenkins, N. & Bossanyi, E. 2001 *Wind Energy Handbook*. John Wiley and Sons.

Butterfield, C. P. 1989 Three-dimentional airfoil performence measurments on a rotating wing. In *EWEC'89 European Wind Energy Conference and Exhibition*.

Carlén, I. 2005*a* Solde - a tool for finite element deflection analysis of wings. *Tech. Rep* TG-R-05-04.

Carlén, I. 2005*b* Structural analysis of wind turbine blades - 3d modelling and slender element approximations. *Tech. Rep* TG-R-05-03.

Charnock, H. 1955 Wind stress on water surface. *Q.J.R. Meteorol. Soc.* **81**, 639–640.

Chaviaropouos, P. K., Nikoalau, I., Aggis, K., Sørensen, J., Montgomerie, B., von Geyr, H., Hansen, M., Kang, S., Voutsinas, S. & Dyrmose, S. 2001 Viscous and aeroelestic effects on wind turbine blades: The viscel project. In *Proceedings of the 2001 European Wind Energy Conference and Exhibition* (ed. P. Helm & A. Zervos). Munchen.

Crespo, A., Hernández, J. & Frandsen, S. 1998 Survey of modelling methods for wind turbine wakes and wind farmes. *Journal of Wind Energy* **2**, 1–24.

Cutler, J., 2004 *History of Wind Energy - Encyclopedia of Energy*, vol. 6. Boston: Elsevier.

Duque, E., van Dam, C. & Hughes, S. 1999 Navier-stokes simulations of the NREL combined experiment phase ii rotor. In *AIAA Paper 99-0037*.

Duque, E., Johnson, W., van Dam, C., Cortes, R. & Yee, K. 2000 Numerical prediction of wind turbine power and aerodynamic loads for the NREL phase ii combined experiment rotor. In *AIAA Paper 2000-0038*.

Ebert, P. R. & Wood, D. H. 1997 The near wake of a model horizontal-axis windturbine-i. experimental arrangement and initial results. *Renewable Energy* **12** (3), 225–243.

Ebert, P. R. & Wood, D. H. 1999 The near wake of a model horizontal-axis windturbine-ii. general features of the three-dimensional flowfield. *Renewable Energy* **18**, 513–534.

Ebert, P. R. & Wood, D. H. 2001 The near wake of a model horizontal-axis windturbine-iii. properties of the tip and root vortices. *Renewable Energy* **22**, 461–472.

Efraimsson, G., Petrini, E. & Nordsröm, J. 2005 Errors in numerical simulations of vortices. *Internal report, TRITA-AVE 2006:90, ISSN 1651-7660*.

Eggeston, D. M. & Stoddard, F. S. 1987 *Wind turbine engineering design*. New York: Van Nostrand Rheinhold.

Eggleston, D. & Starcher, K. 1990 Comparative studies of the aerodynamics of several wind turbines using flow visualization. *J Solar Eng* (39), 112:301–9, division L.

EWEA - *The European Wind Energy Association (www.ewea.org)*, 2008 *Pure Power - Wind Energy Scenarios up to 1030*.

Freris, L. L. 1990 *Wind Energy Conversion Systems*. Cambridge University Press.

Ganander, H. 2005 Method for stability analysis based on the floquet theory and vidyn calculations. *Tech. Rep*.

Glauert, H. 1935 Das maximum der theoretisch möglichen ausnützung des windes durch windmotoren. *Aerodynamic Theory* (4), 169–360, division L.

GWEC - *Global Wind Energy Council (www.gwec.net)*, 2008 *Global Wind Energy Outlook 2008*.

Hand, M., Simms, D., Fingersh, L., Jager, D., Cotrell, J., Schreck, S. & Larwood, S. 2001 Unsteady aerodynamic experiment phase vi: Wind tunnel test configuration and available data campaigns. *Tech. Rep* NREL/TP-500-29955. NREL.

Hansen, M., Sørensen, J., Michelsen, J. & Sørensen, N. 1997 A global navier-stokes rotor prediction model. In *AIAA Paper 97*.

Hirsch, S. K. C. 2001 Features of the 3d viscous flow around wind turbine blades based on numerical solutions. In *Proceedings of the 2001 European Wind Energy Conference and Exhibition* (ed. P. Helm & A. Zervos). Munchen.

Jimenez, A., Crespo, A, Migoya, E. & Garcia, J. 2007 Advances in large-eddy simulations of a wind turbine wake. *Journal of physics: Conference series, The science of making torque from wind* **75** (012041).

Joukowski, N. 1912 Vortex theory of screw propeller. In *Trudy Otd. Fiz. Nauk Mosk. Obshch Lyub. Estest. Antr. Etn*.

Lanchester, F. W. 1915 A contribution to the theory of propulsion and the screw propeller. *Transaction of the Institution of Naval Architects*.

Madsen, H. A. 1996 A CFD Analysis of the Actuator Disc Flow compared with Momentum Theory Results. In *IEA Joint Action - Aerodynamics of Wind Turbines, 10th Symposium, Edinburgh*.

Madsen, H. A. 1999 Yaw Simulation Using a 3D Actuator Disc Model Coupled to the Aeroelastic Code Hawc. In *IEA Joint Action - Aerodynamics of Wind Turbines, 13th Symposium, Stockholm*.

Madsen, H. A. & Rasmussen, F. 1991 Static pressure measurements on a rotating and non-rotating 2.375 m wind turbine blade-comparision with 2d calculations. In *Wind Energy: Technology and Implementation, Amsterdam EWEC'91: Elsevier Science Publishers*.

Mann, J. 1994 The spatial structure of neutral atmospheric surface-layer turbulence. *Journal of Fluid Mechanics* **273**, 141–168.

Mann, J. 1998 Wind field simulation. *Prob. Engng. Mech* **13** (4), 269–282.

Mann, J., Ott, S., Jørgensen, B. H. & Frank, H. P. 2002 Wasp engineering 2000. *Tech. Rep* Risø-R-1356(EN).

Manwell, J. F., McGowan, J. K. & Rogers, A. L. 2002 *Wind Energy Explained, theory, design and application*. John Wiley and Sons.

Massouh, F. & Dobrev, I. 2007 Exploration of the vortex wake behind of wind turbine rotor. *Journal of physics: Conference series, The science of making torque from wind* **75** (012036).

Medici, D. 2005 Experimental studies of wind turbine wakes - power optimisation and meandering. PhD thesis, Dept. of Mechanics, The Royal Institute of Technology, KTH, ISRN KTH/MEK/TR–05/19–SE.

Michelsen, J. & Sørensen, N. 2001 Current developments in navier-stokes modelling of wind turbine rotor flow. In *Proceedings of the 2001 European Wind Energy Conference and Exhibition* (ed. P. Helm & A. Zervos). Munchen.

Michelsen, J. A. 1992 Basis3d - a platform for development of multiblock pde solvers. *Tech. Rep* AFM 92-06. Dept. of Fluid Mechanics, Technical University of Denmark, DTU.

Michelsen, J. A. 1994 Block structured multigrid solution of 2d and 3d elliptic pde's. *Tech. Rep* AFM 94-06. Dept. of Fluid Mechanics, Technical University of Denmark, DTU.

Mikkelsen, R. 2003 Actuator disc methods applied to wind turbines. PhD thesis, Dept. of Fluid Mechanics, Technical University of Denmark, DTU.

Mikkelsen, R., Sørensen, J. N., Øye, S. & Troldborg, N. 2007*a* Analysis of power enhancement for a row of wind turbines using the actuator line technique. *Journal of physics: Conference series, The science of making torque from wind* **75** (012044).

Mikkelsen, R., Sørensen, J. N. & Troldborg, N. 2007*b* Prescribed wind shear modelling with the actuator line technique. In *Proc. of EWEC 2007, European Wind Energy Conference*. Milano.

Montgomerie, B. 2004*a* Methods for root effects, tip effects and extending the angle of attack range to $\pm 180^\circ$, with application to aerodynamics for blades on wind turbines and propellers. *Tech. Rep* FOI-R-1305–SE.

Montgomerie, B. 2004*b* Vortex model for wind turbine loads and performance evaluation. *Tech. Rep* FOI-R–1301–SE. Swedish Defence Research agency, Stockholm Sweden.

Montgomerie, B. & Dahlberg, J-A. 2003 Vortex systems studies on small wind turbines. *Tech. Rep* FOI-R–0936–SE. Swedish Defence Research agency, Stockholm Sweden.

Okulov, V. & Sørensen, J. 2007 Stability of helical tip vortices in a rotor far wake. *J. Fluid Mech.* (576), 1–25.

Rankine, W. J. M. 1865 On the mechanical principles of the action of propellers. *Transaction of the Institute of Naval Architects* **6**, 13–39.

Ronsten, G. 1991 Static pressure measurements on a rotating and non-rotating 2.375 m wind turbine blade-comparision with 2d calculations. In *Wind Energy: Technology and Implementation, Amsterdam EWEC'91: Elsevier Science Publishers*.

Savino, J. & Nyland, T. 1985 Wind turbine flow visaulization studies. In *Proceedings of the Windpower '85 Conference*. American Wind Energy Association, Washington DC.

Schreck, S. 2002 The NREL full-scale wind tunnel experiment introduction to the special issue. *Wind Energy* (5), 77–84.

Shimizu, Y. & Kamada, Y. 2001 Studies on a horizontal axis wind turbine with passive pitch-flap mechanism (performance and flow analysis around wind turbine). *J Solar Eng* (123), 516–22.

Sørensen, J. N. 1986 Three-level, viscous-inviscid interaction technique for the prediction of separated flow past rotating wings. *Tech. Rep* AFM report 86-07.

Sørensen, J. N. 1999 Viscwind viscous effects on wind turbine blades. *Tech. Rep* ET-AFM 9902. Dept. of Fluid Mechanics, Technical University of Denmark, DTU.

Sørensen, J. N. & Kock, C. W. 1995 A model for unsteady rotor aerdynamics. *Journal of Wind Energy and Industry Aerodynamic* **58**, 259–275.

Sørensen, J. N., Mikkelsen, R. & Troldborg, N. 2007 Simulation and modelling of turbulence in wind farms. In *EWEC 2007:Milan, European Wind Energy Association*.

Sørensen, J. N. & Myken, A. 1992 Unsteady actuator disc model for horizontal axis wind turbine. *Journal of Wind Engineering and Industry Aerodynamics* **39**.

Sørensen, J. N. & Shen, W. Z. 2002 Numerical modeling of wind turbine wakes. *Journal of Fluid Engineering* **124**.

Sørensen, J. N., Shen, W. Z. & Munduate, X. 1998 Analysis of wake states by a full-field actuator disc model. *Wind Energy* **1**, 73–88.

Sørensen, N. & Hansen, M. 1998 Rotor performance predictions using a navier-stokes method. In *AIAA Paper 98*.

Sørensen, N. & Michelsen, J. 2000 Aeropredictions for the unsteady aerodynamics experiment phase-ii rotor at the national renewable laboratory. In *AIAA Paper 2000*.

Sørensen, N. N., Michelsen, J. A. & Schreck, S. 2002 Navier-stokes predictions of the NREL phase vi rotor in the nasa ames 80 ft $\times$ 120 ft wind tunnel. *Wind Energy* (5), 151–69.

Sørensen, N. N. 1995 General perpose flow solver applied to flow over hills. PhD thesis, Risø National Laboratory, Roskilde.

Ta Phuoc, L. 1994 Modeles de sous maille appliques aux ecoulements instationnaires decolles. In *Proc. of the DRET conference: 'Aerodynamique Instationnaire Turbulents - Aspects Numeriques et Experimentaux*.

Troldborg, N., Sørensen, J. & Mikkelsen, R. 2007 Actuator line simulation of wake of wind turbine operating in turbulent inflow. *Journal of physics: Conference series, The science of making torque from wind* **75** (012063).

Vermeer, L. 2001 A rewiew of wind turbine wake research at tudelft. In *A Collection of the 2001 ASME Wind Energy Symposium Technical Papers*. New York.

Vermeer, L. J., Sørensen, J. N. & Crespo, A. 2003 Wind turbine wake aerodynamics. *Progress in Aerospace science* (39), 467–510, division L.

Vermeer, N. 1988 Velocity measurements in the near wake of a model rotor (in dutch). In *Fourth Dutch National Wind Energy Conference*. Noordwijkerhout The Netherlands.

Vermeer, N. 1989 Velocity measurements in the near wake of a model rotor. In *European Wind Energy Conference 1989*. Glasgow UK.

Vermeer, N. & van Bussel, G. 1989 Velocity measurements in the near wake of a model rotor and comparison with theoretical results. In *Fifteeth European Rotorcraft Forum*. Amsterdam The Netherlands.

de Vries, O. 1979 Wind-tunnel tests on a model of two-bladed horizontal axis wind turbine and evaluation of an aerodynamic performance calculation method. *Tech. Rep* NLR TR 79071 L. NLR, Amsterdam.

Wallin, S. & Girimaji, S. S. 2000 Evolution of an isolated turbulent trailing vortex. *AIAA* (38), 657–665.

Walther, J., Guénot, M., Machefaux, E., Rasmussen, J. T., Chatelain, P., Okulov, V. L. & Sørensen, J. N. 2007 A numerical study of the stability of vortices using vortex methods. *Journal of physics: Conference series, The science of making torque from wind* **75** (012034).

Watters, C. S. & Masson, C. 2007 Recent advantages in modeling of wind turbine wake vortical structure using a differential actuator disc theory. *Journal of physics: Conference series, The science of making torque from wind* **75** (012037).

Whale, J., Anderson, C. G., Bareiss, R. & Wagner, S. 1996 A study of the near wake structure of a wind turbine comparing measurements from laboratory and full-scale experiments. *Solar Energy* **56** (6), 621–33.

Widnall, S. 1972 The stability of a helical vortex filament. *J. Fluid Mech.* (54(4)), 641–663.

Wilson, R. E. 1998 *Aerodynamic behavior of wind turbines*.

Wilson, R. E. & Lissaman, P. B. S. 1976 Aerodynamic performance of wind turbines. In *Energy research and development administration, ERDA/NSF/04014/1*.

Wussow, S., Sitzki, L. & Hahm, T. 2007 3d simulation of the turbulent wake behind a wind turbine. *Journal of physics: Conference series, The science of making torque from wind* **75** (012033).

Xu, G. & Sankar, L. 1999 Computational study of horizontal axis turbines. In *AIAA Paper 99-0042*.

Xu, G. & Sankar, L. 2000 Effects of transition, turbulence and yaw on the performance of horizontal axis wind turbines. In *AIAA Paper 2000-0048*.

Zahle, F. & Sørensen, N. N. 2007 On the influence of far-wake resolution on wind turbine flow simulations. *Journal of physics: Conference series, The science of making torque from wind* **75** (012042).

Åhlund, K. 2004 Investigation of the NREL nasa/ames wind turbine aerodynamics database, engineering degree thesis. *Tech. Rep*.